UNIVERSITY OF CALIFORNIA,

IRVINE

Turbulent Transport of Fast Ions Due To Magnetic Flux Ropes

DISSERTATION

submitted in partial satisfaction of the requirements
for the degree of

DOCTOR OF PHILOSOPHY

in Physics

by

Adam Preiwisch

Dissertation Committee:
Professor William Heidbrink, Co-chair
Professor Roger McWilliams, Co-chair
Professor Zhihong Lin

2015

TABLE OF CONTENTS

LIST OF FIGURES

LIST OF TABLES

ACKNOWLEDGEMENT

I am thankful for the help and support I've received from many people over the last few years. Without them, none of this would be possible. Their expertise, guidance, thoughtful criticisms, and obvious experience have helped to shape my research and graduate experiences in myriad positive ways. I'm am grateful for the continued support received by my advisors Professor William Heidbrink and Professor Roger McWilliams. I owe you both sincere thanks for your guidance and willingness to pass on substantial amounts of your scientific knowledge. You did so with great patience, enthusiasm, and compassion. Your work has grown my skills in ways I never knew a mentorship could. For that, I am sincerely thankful.

The staff and research scientists at the Large Plasma Device at UCLA have also been an amazing source of support and guidance throughout the experimental design and data acquisition portions of this project. They graciously shared their facility and volunteered their time; their help has been of paramount importance to these works. Steve Vincena, Shreekrishna Tripathi, and Bart Van Compernolle offered continuous facility and hardware support for the duration of the experiments runtime on the machine. They were always available to help troubleshoot issues and offer thoughtful criticisms of various design elements of the experiment. Walter Gekelman, Tim DeHaas, Patrick Prybil, and Troy Carter similarly made themselves available for discussions on the flux rope interactions and device hardware. Additional staff, specifically Marvin Drandell and Zoltan Lucky provided assistance troubleshooting issues and offering guidance throughout our experiments.

Early work in the UCI Fast Ion group was under the supervision of Dr. Shu Zhou. I began this

research project with his help, and I am immensely thankful for his contributions. His past design and programming work has formed the basis for portions of this experiment. Further, his help learning the coding routines associated with the group's simulation routine has proven invaluable. Dr. Heinrich Boehmer has similarly helped throughout these works. He has provided continued support in the form of thoughtful ideas/criticisms related to experimental and hardware design, help revising works, discussions on benchmarking hardware, and too many other contributions to list here.

Last, but certainly not least, I'd like to thank my immediate family for their support. My parents Karl and Maria have been terrific parents throughout my time in graduate school, never hesitating to offer a hand or lend an ear. Thanks for everything.

Curriculum Vitae

FIELD OF STUDY:

Experimental Plasma Physics

EDUCATION:

Ph. D. in Plasma Physics,
University of California, Irvine 2011-2015

M.S. in Plasma Physics,
University of California, Irvine 2009-2011

B.S. in Applied Physics,
University of Minnesota – Twin Cities 2005-2009

B.A. in Astrophysics
University of Minnesota – Twin Cities 2005-2009

PUBLICATIONS

"Fast ion transport due to flux ropes in the large plasma device" A. Preiwisch, W. W. Heidbrink, R. McWilliams, H. Boehmer, B. Van Compernolle, S. Vincena, S. K. P. Tripathi, T. De Haas, W. Gekelman, *Physics of Plasmas*, pending (2015).

"Measurements of interactions between waves and energetic ions in basic plasma experiments" W. W. Heidbrink, H. Boehmer, R. McWilliams, A. Preiwisch, Y. Zhang, L. Zhao, S. Zhou, A. Bovet, A. Fasoli, I. Furno, K. Gustafson, P. Ricci, T. Carter, D. Leneman, S. K. P. Tripathi and S. Vincena, *Plasma Physics of Controlled Fusion* **v54**, 124007 (2012).

PRESENTATIONS

"Fast Ion Transport By Magnetic Flux Ropes" Poster, American Physical Society-Division of Plasma Physics, New Orleans, Oct. 2014, Adam Preiwisch

"Experiment to measure fast ion transport by magnetic fluctuations" Poster, American Physical Society-Division of Plasma Physics, Denver, Nov. 2013, Adam Preiwisch

LIST OF SYMBOLS

B_0	Ambient Magnetic Field
dz_{port}, dport	Distance Between Two Diagnostic Ports at LAPD
$D_\perp$	Diffusion Coefficient in Perpendicular Direction (To the Magnetic Fields)
e	Electronic Charge
I_{sat}, ISAT	Ion Saturation Current
k_B	Boltzmann's Constant
$k_\parallel$, k_z	Wave Vector Component Parallel To B0
$k_\perp$	Wave Vector Component Perpendicular To B0
m	Mass; Wave Mode Number
M_i	Mass of Thermal Plasma Ions
n_e	Electron Density
n_i	Plasma Ion Density
t	Time
T_e	Thermal Electron Temperature
T_i	Thermal Ion Temperature
T_f	Fast Ion Cyclotron Period
v_{perp}, $v_\perp$	Velocity Component Perpendicular To Magnetic Field
v_z	Velocity Component Parallel To Magnetic Field
v_e	Thermal Electron Velocity
v_i	Thermal Ion Velocity
v_f	Fast Ion Velocity
V_f	Plasma Floating Potential
V_p	Plasma Potential
z	Axial Position In The LAPD Parallel To B0
δB	Magnetic Fluctuation Intensity
δE	Electrostatic Fluctuation Intensity
ϕ	Electric Potential
ε	Permittivity Of Free Space
θ	Pitch Angle of the Fast Ion Beam
θ_x	Cross Phase Between Two Signals
ω, ω_{ci}	Plasma Ion Cyclotron Frequency
ρ_i	Thermal Ion Gyro Radius
ρ, ρ_f	Fast Ion Gyro Radius
ρ_e	Thermal Electron Gyro Radius
ρ_s	Thermal Ion Sound Radius
τ_{PAS}	Pitch Angle Scattering Time
τ_{slow}	Slowing Down Time
$\chi 2$	Chi Square Test
μ_0	Permeability Of Free Space
Ω, Ω_f	Fast Ion Gyro-Frequency

Abstract of the Dissertation

Turbulent Transport of Fast Ions Due To Magnetic Flux Ropes

By

Adam Preiwisch

Doctor of Philosophy in Physics

University of California, Irvine, 2015

Professor William Heidbrink, Co-chair

Professor Roger McWilliams, Co-chair

The transport of fast ions in magnetic flux ropes in a laboratory plasma is studied. Strong perturbing flux ropes (δE ~175 V/m, δB ~7 G) are generated by secondary cathode-anode pair at the upgraded LArge Plasma Device (LAPD). A 500-1000 eV lithium ion test beam is passed through the turbulent region and recollected by a gridded collimated analyzer, revealing enhanced fast ion broadening attributable to flux rope perturbations. The broadening is observed to be well in excess of Coulomb scattering levels. Monte Carlo simulation is performed with model electrostatic and magnetic fields, revealing negligible spreading as a result of the magnetic perturbations. Modeled electrostatic perturbations are observed to broaden the beam by 3.0 mm^2 at the closest recollection plane, increasing as the transit time squared further downstream. Transport attributed to electrostatic fluctuations has been shown to decrease with energy while magnetic transport does not. Enhanced fast ion transport observed during the flux rope off phase is presently unexplained.

Chapter I
Introduction

1.1 Fast Ion Transport in Flux Ropes

Mechanisms that enhance the transport of fast ions are of particular interest in space, fusion, and laboratory plasmas. Electromagnetic waves are ubiquitous in space plasma, and cause stability issues in potential fusion reactors necessitating careful study of their effects and interactions with fast ions. Understanding the nature and magnitude of these interactions has attracted growing interest in recent years. Laboratory studies of these interactions are useful when in situ studies are unable to be performed.

Past work performed on the LAPD at the University of California, Los Angeles (UCLA) has focused on conducting laboratory plasma experiments designed to enhance understanding of transport mechanisms and wave structure. The LAPD scientists and support staff have demonstrated the ability to create magnetic flux ropes in a laboratory environment. [1] The flux ropes are helical magnetic fields generated by pulsing on two current channels with the use of an auxiliary cathode/anode which is independent of the plasma source. A LaB_6 cathode is masked with a carbon sheet that has two holes in it. The flux rope currents are emitted from the exposed cathode emission area. The flux ropes twist and rotate about each other and the central magnetic axis. [2] The ropes are observed to be kink-unstable at lower background magnetic fields (approximately 330 G). [3] Recent past work has focused on the creation of hardware to generate sets of rotating axially-propagating flux ropes. [4] Analysis of probe data shows increased electron temperature within the flux ropes. The ropes are, in essence, Alfvenic in structure; their currents propagate at the Alfven speed when they are switched on. [3] While the

ropes are line tied to their cathode, they are observed to merge at axial distances a few meters downstream from the cathode. The data are averaged using a conditional trigger and field line maps show that the steady state behavior of the ropes is rotation about the magnetic axis as they twist around each other. [5] Interactions of ions with energies much greater than thermal energies with these filamented magnetic structures are explored in this work.

1.2 Fast Ion Transport Project at UC Irvine

The fast ion transport project at UC Irvine started in September 2004. The project is supported by the Department of Energy (DOE) and has been renewed three times. Funded at $100k per year, the project aims to study a variety of aspects of the fast ion transport in the Large Plasma Device, including classical transport, transport by electrostatic waves, transport by electromagnetic waves, and transport by magnetic flux rope. Three Ph. D. students have graduated in this project: Dr. Liangji Zhao (2003-2005) has worked on the classical fast ion transport during the low-density afterglow plasmas in the LAPD. Dr. Yang Zhang (2004- 2008) has worked on the fast-ion resonance with shear Alfvén waves and the spectral gap of shear Alfvén waves in a periodic array of magnetic mirrors. Dr. Shu Zhou (2007-2011) has worked on the transport of fast ions and thermal plasmas in low-frequency, electrostatic microturbulence. This thesis work (2011-2015) focuses on the transport of fast ions interacting with warm, filamented electron structures known as magnetic flux ropes.

In this thesis work, we have extensively studied the interaction between the fast ion test particle beam and the combination of electrostatic and magnetic turbulence generated by magnetic flux ropes. A Physics of Plasmas paper on the material presented herein is currently in the process of being published. Fast ion hardware has been resurfaced by a plasma cleaning process employed by staff at UC Irvine. Fast ion gun biasing grids have also been replaced during the course of

this experiment. We closely collaborate with research teams from the Basic Plasma Science Facility at UCLA, and the École Polytechnique Fédérale de Lausanne (EPFL). We have presented papers at various domestic and international conferences.

1.2.1 Classical Transport of Fast Ions in Plasmas

Classical fast ion transport was initially investigated in the afterglow of the LAPD (Dr. Liangji Zhao, 2003-2005). A 3 cm diameter RF ion gun launched a pulsed, ~300 eV ribbon shaped argon ion beam parallel to the magnetic field in the LAPD. The parallel energy of the beam was measured by a two-grid energy analyzer at two axial locations ($z = 0.32$ m and $z = 6.4$ m) from the ion gun in the LAPD. To measure cross-field transport, the beam was launched at 15 degrees to the magnetic field. To avoid geometrical spreading, the beam parameters were chosen such that the ion beam was periodically focused at axial locations accessible to probes. Radial beam profile measurements were performed at these axial locations. The measured cross-field transport is in agreement to within 15% with the analytical classical collision theory and the solution to the Fokker-Planck kinetic equation. Collisions with neutrals have a negligible effect on the beam transport measurement but attenuate the beam current. The beam energy distribution measurements were calibrated by LIF (laser induced fluorescence) measurements performed in the Irvine Mirror.

1.2.2 Radial Shifts of Fast Ions Due To Electric Fields

Radial shifts of fast ion beams due to electric fields was investigated in the LAPD (Dr. Shu Zhu, 2007-2011). A Lithium ion test beam with energy varied from 415-1000 eV is generated in background Helium plasma in the LAPD. By applying a bias voltage (75-150 V) to an annulus obstacle located in the device, radial electric fields were generated in the vicinity of the orbiting ion beam. Interaction with the radial electric field is observed to produce a radial drift of the

beam. Both the magnitude and direction of the centroid drift are in agreement with a Monte Carlo simulation that launches fast ions with an initial spread in real/velocity space and a random phase relative to the wave. Measured field data were used in the simulation.

1.3 Content of Thesis

This thesis covers an experiment on fast ion transport in magnetic flux ropes. Chapter 2 introduces the experimental apparatus, including the LAPD, the fast-ion source and diagnostic tools, and the data analysis methods. Chapter 3 discusses the experimental results: field profiles and line scans for plasma parameters are presented in addition to energy- and time- scaling of the fast ion beam cross-field transport. Chapter 4 discusses the simulation and modeling methods developed to a complementary simulation; a direct comparison to experimental data is presented. A conclusion to this thesis work and future work in the next phase of the fast-ion project is stated in Chapter 6.

Chapter 2
Experimental Apparatus

2.1 LArge Plasma Device at the Basic Plasma Science Facility

The majority of this experiment is carried out at the Basic Plasma Science Facility (BAPSF) located within the University of California, Los Angeles. The facility performs frontier-level research on plasma with applications ranging from fusion energy to space physics. Our work is conducted on the upgraded LArge Plasma Device (LAPD) at the BAPSF; the upgraded LAPD offers the ability to create a ~20 meter long, 75 centimeter diameter, magnetized plasma at a repetition rate of 1 Hz. [6] The background (axial) field is generated by an array of magnetic field coils along the length of the machine and can generate a background field up to 3.5 kiloGauss, though this experiment will only look at particles traveling through fields ranging from 500 Gauss to 1000 Gauss.

The LAPD offers convenient probe access at over 450 access ports via circular and rectangular ports; circular ports are situated roughly every third of a meter along the length of the device. Larger equipment such as our ion gun or flux rope hardware are constrained to use larger rectangular ports, which are available every 5 or 6 ports (roughly every 2 meters).

A primary Oxygen-coated cathode/anode located at one end of the machine generates energetic electrons (around 60 eV) used to ionize the background plasma (typically Helium or Argon) once a second for a duration of ~10 milliseconds. [7] Nominal values for the primary discharge are 4 kA at 60 V bias. Microwave interferometers located at various positions along the length of the device allow the acquisition of density data during the discharge.

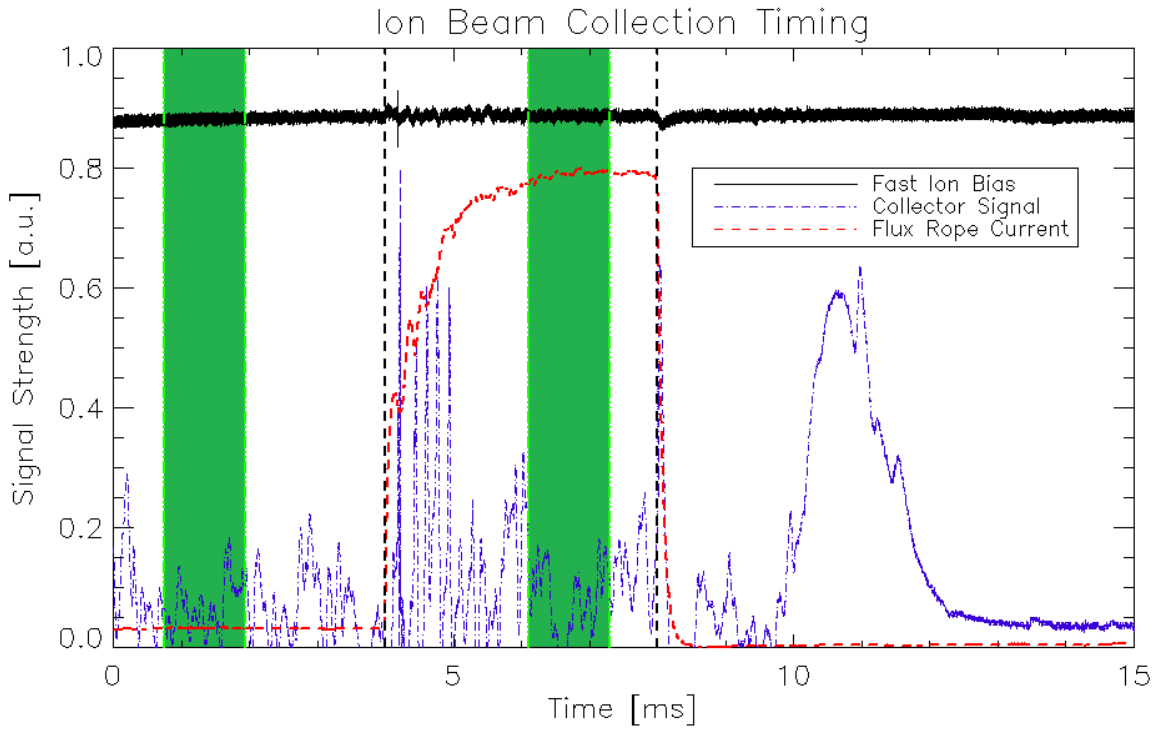

Figure 2.1.1 Ion beam collection timing. Black vertical dashed lines represent flux rope turn on and turn off times. Shaded green regions represent time bins for data averaging. The first bin represents fast ion beam data in the absence of flux rope discharge, while the latter represents beam recollection during active flux rope discharge.

Figure 2.1.2 Picture of the upgraded Large Plasma Device at the BAPSF. The purple coils shown are responsible for generating the axial magnetic field. Smaller probes are inserted into flanges attached to circular ports, while larger equipment requires rectangular port access (not shown).

Various probes are introduced into the LAPD through available circular ports and are interfaced with the data acquisition system. Probe positioning is controlled locally by a workstation supplying movement commands between shots. Probes typically take numerous shots at each spatial location while moving through a series of positions across an (x,y) plane at a fixed axial position (z).

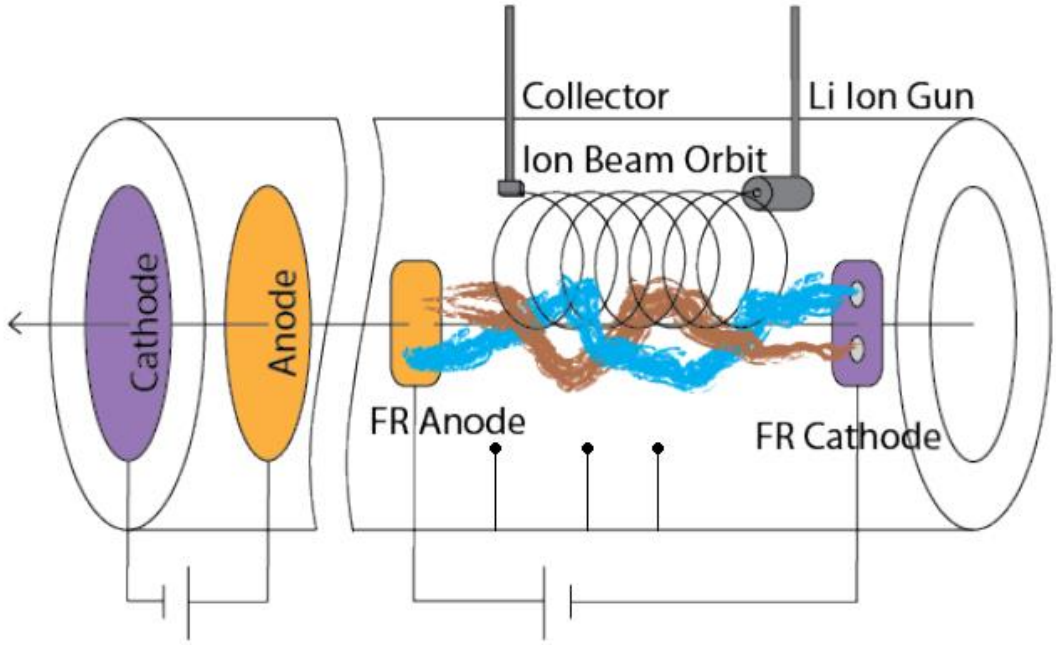

Figure 2.1.3 Experimental layout. Magnetic flux ropes are schematically illustrated as brown/blue channels along the magnetic axis. The nominal ion beam orbit transits through the active region near the magnetic axis for some fraction of each orbit prior to collection. The separation between the cathode and anode system which generates the ropes is 10 m. The separation of the BaO Cathode that generates the background plasma and its anode is 50 cm.

2.2 BAPSF Diagnostic Tools and Equipment

Various hardware and diagnostic tools were provided by the researchers and support staff at the BAPSF. Necessary hardware such as microwave interferometers, digital oscilloscopes, b-dot and Langmuir probes, and high-speed cameras have been generously provided for use during the

course of this experiment.

2.2.1 Langmuir Probe

Langmuir probes, which exist in numerous configurations, generally allow for the determination of electron temperature, density, potential, and associated fluctuations of a plasma. [8] For our experiment, we relied on two specific implementations of the Langmuir probe: the triple and swept Langmuir probes. While the swept probe is particularly useful in obtaining accurate measurements of electron temperature and density, applying a time-dependent voltage to the single-tip design prevents any meaningful fluctuation data from being obtained, requiring use of both probe types in this experiment.

The triple Langmuir probe consists of a set of three electrodes. Two electrodes are biased to fixed voltages while the third is left floating. The biased electrodes collect positive(/negative) currents. The ion current measured is known as the ion saturation current (ISAT) while the opposite current is proportional to ESAT. The third (floating) electrode is responsible for the floating potential measurement. Triple probe measurements are related to electron temperature and density via:

$$T_e = e(V_e - V_{float})/(\ln 2 \cdot k_B) \quad (2.1)$$

$$n_e = ISAT/(S \cdot e \cdot \mathrm{sqrt}(k_B \cdot T_e/M_i)) \quad (2.2)$$

where S is the surface area of the electrode, ISAT is the observed ion saturation current, V_e is voltage of the negative electrode, and V_f is the voltage of the floating electrode.

In our experiment, the Langmuir triple probe is interfaced with the "Vincena Triple Probe Box" designed and maintained by Steve Vincena. The nominal impedance of the box is ~300 Ohms.

We run this equipment in series with a 20 Ohm resistor, yielding an effective resistance of ~19 Ohms.

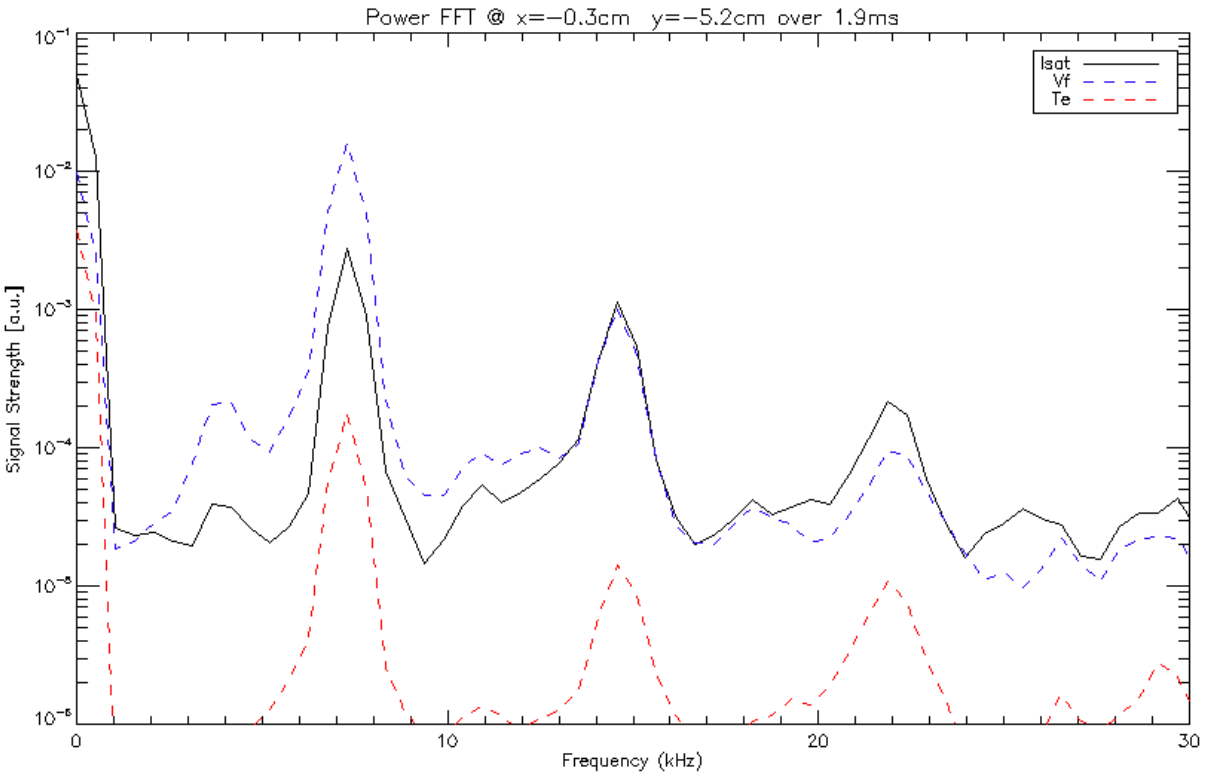

Figure 2.2.1 FFT traces of the power spectra obtained for ISAT, floating potential, and electron temperature via triple probe.

The swept Langmuir probe, on the other hand, generally consists of a single electrode with a time-dependent bias voltage. The action of sweeping through different bias voltages generates an I-V trace that can be used to find electron temperature in the tail/bulk regions, plasma potential, collected current, and equilibrium values for density.

In our experiment, we swept from -77 V to +48 V over the course of 80 μs with a delay of 250 μs between sweeps. The data was acquired over 10 repeated shots. Voltage sweeping began 1 ms prior to the turn on of the flux ropes and continued until the discharge terminated.

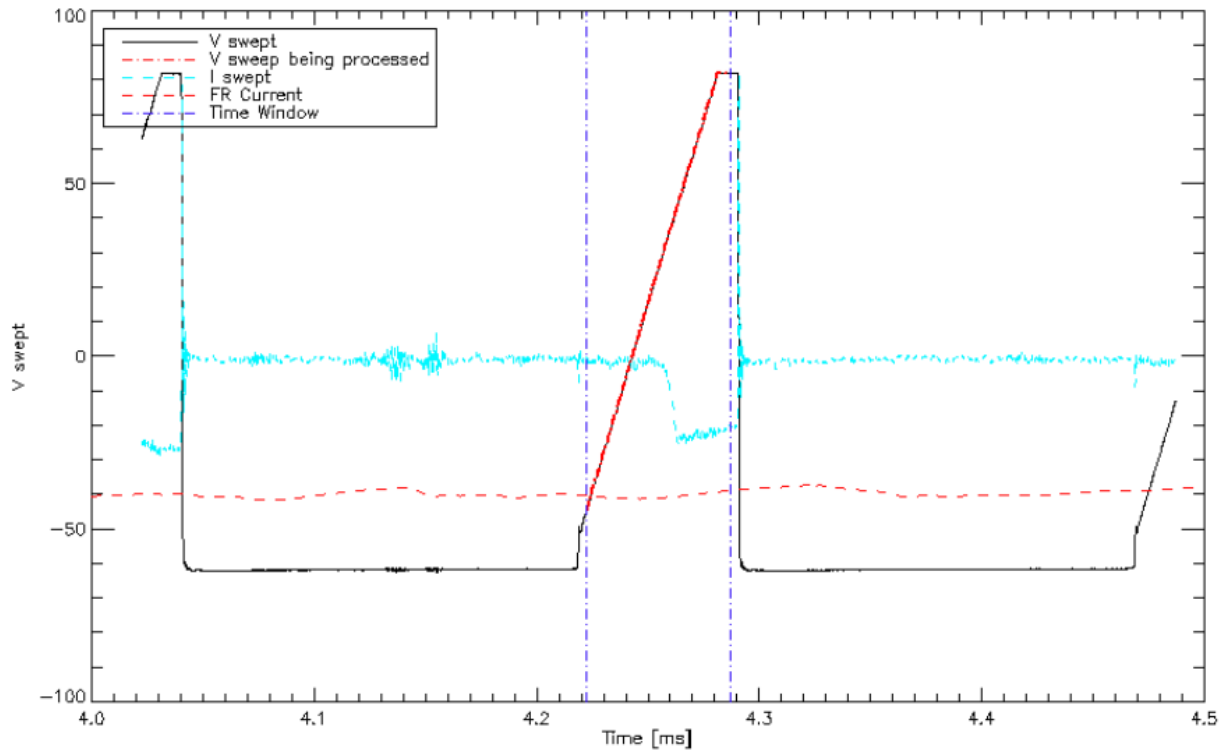

Figure 2.2.2. Time trace of swept probe data prior to flux rope discharge. Individual sweeps last for 80 μs and are generated at a rate of 4 kHz.

2.2.2 B-dot Probe

B-dot probes are used to find the flux rope magnetic field profile as well as the magnitude of magnetic fluctuations. Following the classical magnetic pickup coil design, B-dot probes consist of three orthogonal sets of wound magnetic coils situated within the probe tip that detect magnetic fluctuations via Faraday induction. [9] The obtained signal is passed down the probe shaft to a differential amplifier before output to the data acquisition system. Electrostatic effects are minimized by using two counter-wound coils and subtracting the signals from each other –

effectively subtracting out the electrostatic contribution while doubling the magnetic contribution. The probe is sensitive to signals on the order of a kiloHertz up to roughly 50 MHz.

2.3 Irvine Fast Ion Sources and Detectors

2.3.1 Lithium-Aluminosilicate Ion Source and Ion Gun

The UC Irvine fast ion group has developed and maintained an ion beam source for use in this experiment. Functionally, the ion gun works by introducing a heater circuit with attached ion source into a plasma-immersed vacuum chamber. The source is obtained via commercial vendor Heatwave Labs (model 101142), and includes a modified ground connection between one lead of the heater circuit and the ion source heat shield, consisting of a Mo wire attached between Mo heater lead and Mo heat shielding. The modification was performed at the time of manufacture by a Heatwave Labs engineer.

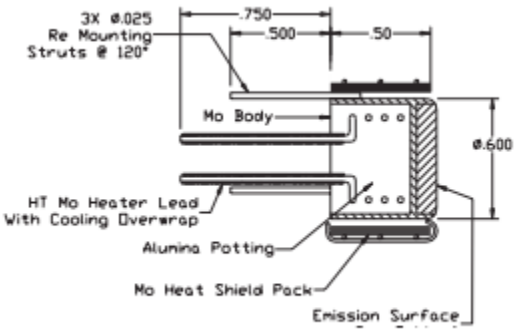

Figure 2.3.1 Schematic of the 101142 Lithium ion source from Heatwave Labs. [10]

Supplying current to the Molybdenum leads of the heater circuit in the presence of biased grids acts to emit Lithium 7 ions deposited into the Aluminosilicate potting; the source is capable of yielding current densities of 1-10 mA/cm^2 at an operating temperature between 950° C and 1100° C. [10] However, the ion gun includes an 5 mm aperture limiting the emission current

density to ~100 μA/cm^2 when operated at a heater current of 11.5 A (~100 W of power). [11] The ion sources are observed to have lifetimes on the order of ~20 hours, necessitating careful use of this resource.

Biased gridding within the ion gun allows the ion beam to be emitted at a known energy, dependent upon the applied voltage. An acceleration-deceleration scheme can be employed, wherein a grid near the source is biased negatively to draw more emission current without modifying the observed energy of the beam. For the duration of this experiment, the first grid has been left grounded to the ion source. The ion beam is observed to have angular divergence on the order of 3 degrees and energy divergence of less than 5 percent when launched into a magnetic field-free vacuum.

The ion gun is timed in such a way as to emit Lithium ions every other shot (at a rate of 0.5 Hz) for a duration of ~20 milliseconds. This allows one run to nearly simultaneously acquire beam on and beam off data during sequential plasma pulses. Data acquisition is typically repeated 10 times (5 on, 5 off) at any individual spatial location in order to reduce noise and ensure reproducibility.

Figure 2.3.2 Picture of the ion gun housing. [11] The Lithium ion source can be seen in the absence of the 5mm aperture. Leads for the heating circuit and biased grids run out through the ion gun shaft.

2.3.2 Particle Collector

The collector probe consists of a conducting collection plate that is recessed within a collimated channel protected by a biased grid. The collimation helps to discriminate against incident particles that do not have similar pitch angle relative to the orientation of the collector – the angular acceptance is found to be ±15°. The biased gridding incorporates a two-grid design not unlike that of the ion source, though the motivation is quite different. Biasing of the two grids to negative/positive voltages allows for the rejection of electrons and lower energy thermal ions, respectively. Nominal biasing voltages for this experiment are up to 46 V(/54 V) on the negative(/positive) grid. The collector was interfaced with the data acquisition system at the LAPD, taking care to minimize noise by using short cables.

2.4 Flux Rope Generation

Hardware capable of generating magnetic flux ropes has been developed by BAPSF staff at UCLA. [3] Additionally, foundational work regarding discharge behavior, stability and safe operating regimes, and electron source replacement were conducted by research and support staff. [1] [4]

2.4.1 Flux Rope Cathode/Anode

A second cathode and anode pair is introduced towards the opposite end of the LAPD; the cathode is inserted into rectangular port 47 whereas the anode is downstream at port 13. The cathode heating element consists of a 8.25 cm diameter LaB6 disk heated to ~1700° C. A carbon mask is situated in front of the cathode, dictating the emission structure of the electrons. Masks

of varying geometry can be created; this experiment uses a “two moon” mask, containing two D-shaped channels with individual diameters of 2.5 cm.

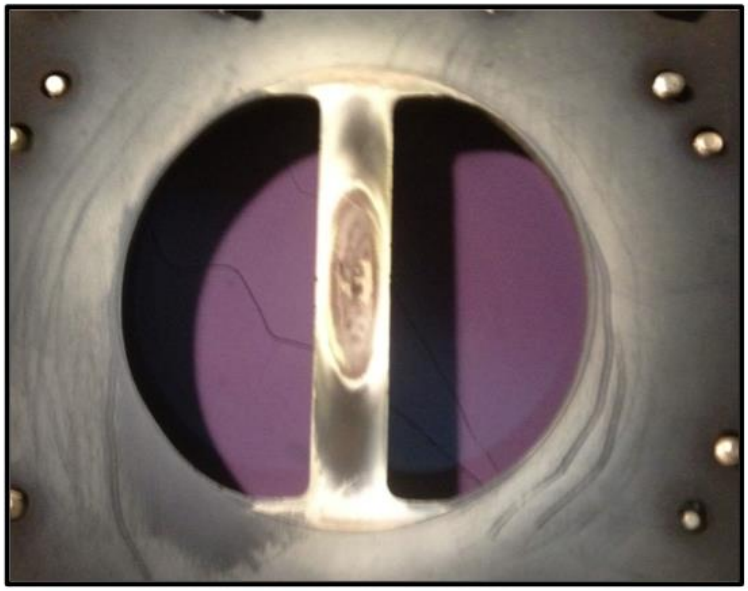

Figure 2.4.1 Picture of the “two moon” flux rope mask.

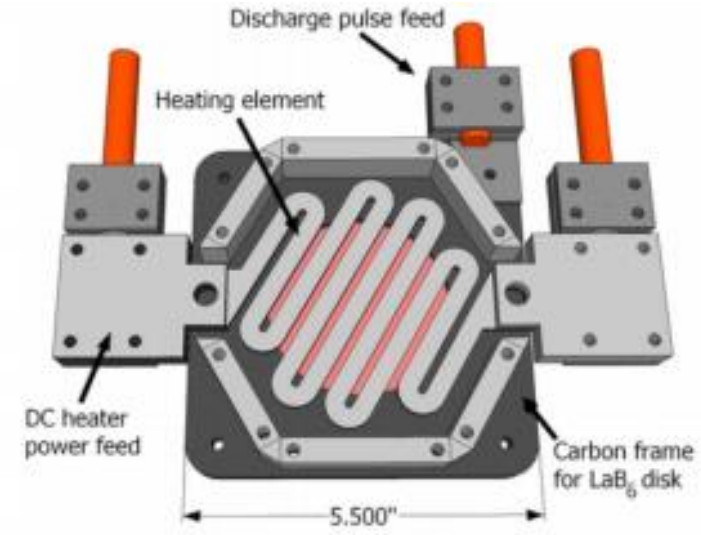

Figure 2.4.2 Diagram of the flux rope cathode design. [4] The winding heating element is hidden behind a carbon mask that dictates the size/shape of the emitted flux ropes.

The anode is situated downstream of the LaB6 cathode and consists of a 70% transparency molybdenum wire mesh. The anode is roughly 25 cm tall by 28 cm wide. [3] The secondary anode is floating with respect to the plasma.

The presence of the cathode's mask generates distinct rope-like channels of electrons that travel axially while rotating about the magnetic axis. The radius of rotation is observed to increase as the electron rope propagates downstream. The frequency of rotation for the flux ropes is determined by FFT of the magnetic field time traces, yielding an apparent rotational frequency of 7.2 kHz. Previous work has predicted that the rotation frequency is approximately equal to $f_{rot} = v_z \cdot B_\theta / 4 \cdot \pi \cdot a \cdot B_z$, [4] where v_z is the axial speed of the flux rope electrons, B_θ is the perpendicular magnetic field, a is the perpendicular scale length, and B_z is the amplitude of the background magnetic field associated with the rope. For our numbers, $v_z \sim c_s \sim 1.4 \times 10^6$ cm/s, a ~ 1.25 cm, B_θ ~ 7.4 G, B_0 ~ 700 G, this yields a frequency of ~1 kHz, which is clearly inconsistent with direct observation.

The LaB_6 cathode is pulsed on for ~4 ms during each LAPD discharge, allowing for data to be taken before, during, and after the flux rope event. Experimental evidence suggests the rope becomes completely unstable and has formation problems below 330 Gauss. In comparison to the LAPD's primary discharge of ~100 W/cm^2, the flux rope discharge is notably higher intensity at $\geq$ 700 W/cm^2. [3] For the two moon case, the nominal discharge parameters for the flux rope cathode are a 160 V discharge at ~110 Amps. Additionally, the resulting temperature profile shows a notable increase to a temperature on the order of ~10 eV (up from a background value of ~3 eV) in the flux rope region. [1]

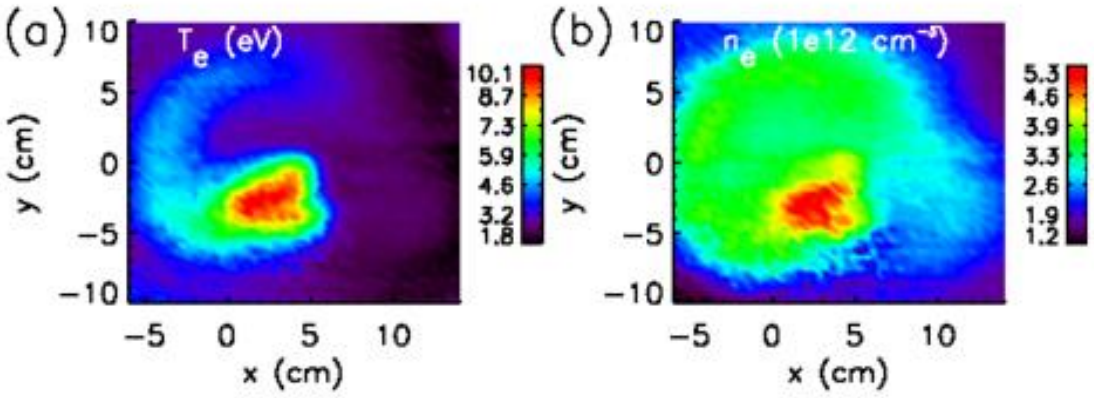

Figure 2.4.3 Profile of the observed electron temperature (a) and density (b) in the presence of flux ropes. Nominal background values in the absence of flux ropes were found to be ~3 eV and 2.5e12 cm^{-3}. [4]

2.5 Data Analysis Methods

Analysis of the collected data is of paramount importance to understanding the results. LAPD data is used in conjunction with IDL-based programming routines to sort through and process the plethora of data obtained.

2.5.1 Langmuir Probe Analysis

2.5.1.1 Triple Probe Analysis

For two triple probes taking data simultaneously at separate spatial locations, cross-correlation analysis can be employed to find the cross-spectrum of two individual Fourier transforms:

$$S_{xspec}(\omega,x,y) = f_1(\omega,x,y)\cdot f_2^*(\omega,x,y) \qquad (2.4)$$

With cross-phase and cross-coherency given by:

$$\theta = \arctan(\ \text{Imaginary}(S_{xspec}) \,/\, \text{Real}(S_{xspec})\ ) \qquad (2.5)$$

$$\langle\gamma^2\rangle = \langle S_{xspec} \cdot S^*_{xspec}\rangle \,/\, (f_1 \cdot f_1^*)(f_2 \cdot f_2^*) \qquad (2.6)$$

Further analysis of the cross-phase in frequency space can illuminate mode structure. This process is carried out for triple probe data acquired via one moving probe and one fixed probe separated by a known distance. This allows the creation of 2D planes of data to visualize temperature, density, and potential fluctuations.

2.5.1.2 Swept Probe Analysis

Swept probe data necessarily loses meaningful time resolution as a result of using timed voltage sweeps to acquire data. This technique produces I-V traces at each spatial location along similar 2D planes. Fitting exponential decay trends to the I-V curves allows for the determination of temperatures in the bulk/tail of the plasma. ISAT and ESAT can be found by direct fitting of the I-V curves.

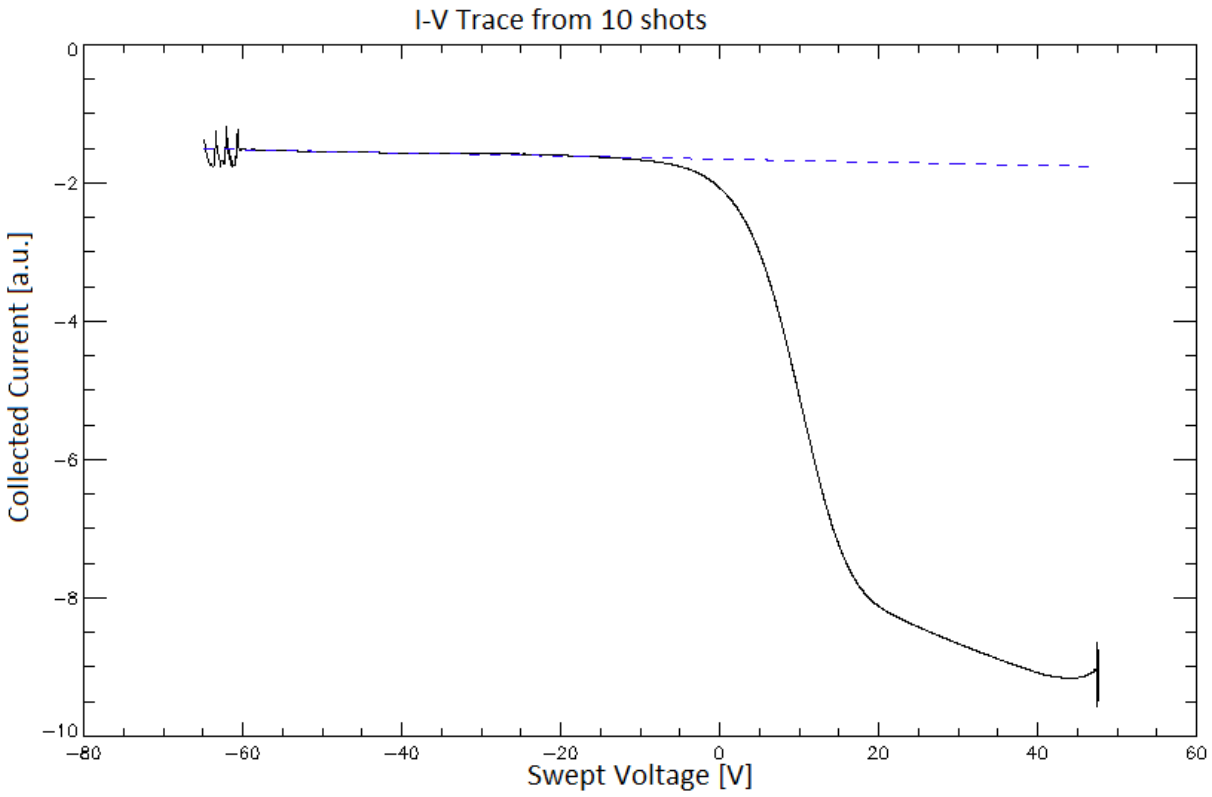

Figure 2.5.1 Example of an I-V curve generated at one spatial position from 10 consecutive shots. Bulk(/tail) electron temperature is found by fitting exponential deviation from linear fits to ISAT(/ESAT).

2.5.2 B-dot Signal Analysis

The nominal signal obtained via B-dot probe is the time-derivative of the magnetic field for each coil, yielding derivatives of (B_x, B_y, B_z) or (B_φ, B_θ, B_z). The resulting values for the magnetic field can be obtained by an integration routine through IDL. After defining a calibration function and subtracting background signal, the time trace can be transformed into frequency space. Upon application of the calibration function, the signal is numerically integrated before inverting the transformation. A low frequency filter is sometimes used to reduce noise.

2.5.3 Beam Profile Analysis

Collector signals representing the observed fast ion intensity at any given position are relayed to the data acquisition system via BNC cable in the form of voltage readings. Typically, the fast ion current is measured through a 1 MΩ resistor prior to amplification by a differential amplifier. [12]

As previously remarked in the ion gun section (see 2.3.1), collected data is divided into "beam on" and "beam off" results. The "beam off" signals represent the background collection in the absence of fast ions, and are thus background subtracted from the "beam on" data. Doing so for data taken over an (x,y) plane yields a beam contour in (x,y) or (r,φ) space. Nominally, all shots are included in this procedure.

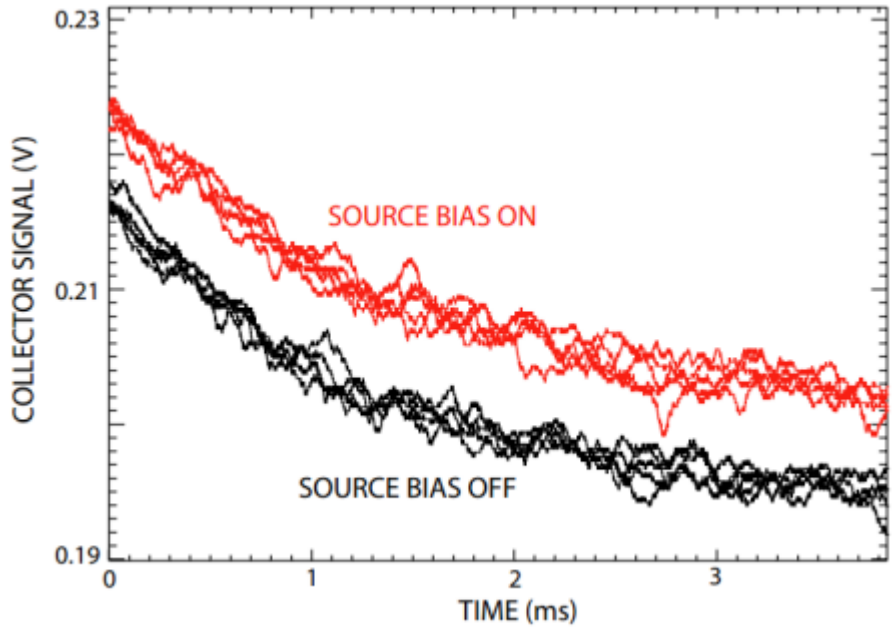

Figure 2.5.1 Plot showing a short time trace of "beam on" and "beam off" for a collection of 10 shots. The difference between the two signals is taken over the array of data. [7]

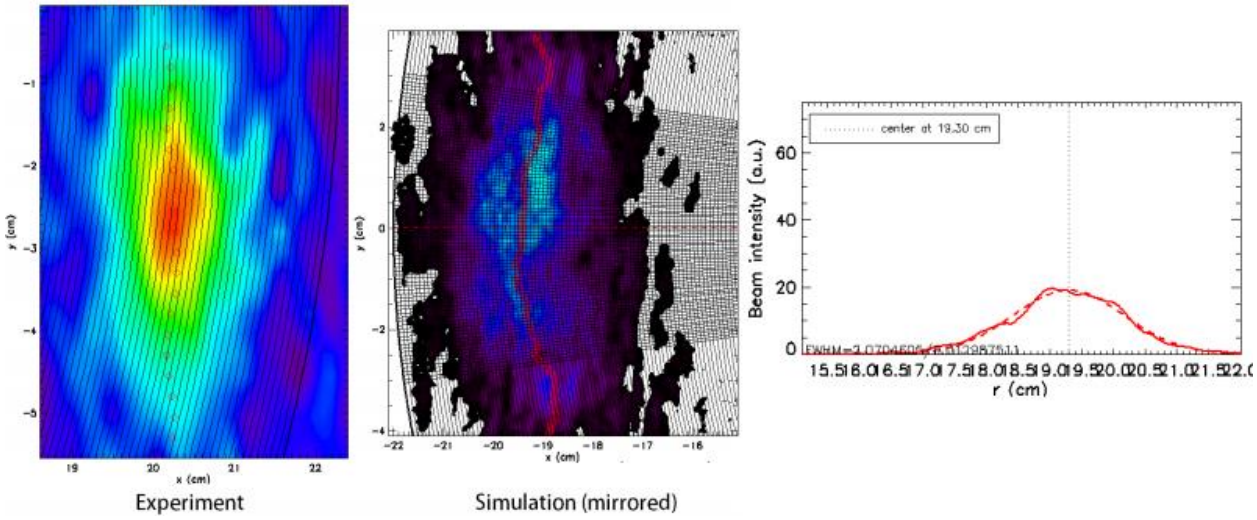

Figure 2.5.2 Comparison of simulated beam spot to experimental data. The left contour shows the observed beam spot after background subtraction and shot averaging. Radial FWHM fitting of the weighted radial profile. The routine works for both LAPD data as well as simulated results, allowing for direct comparison.

Once beam data has been obtained, fitting routines are employed to determine the radial and angular width of the ion distribution. Our present surveys are primarily concerned with radial beam spreading since our collector is well-suited to detecting radial changes on the order of 1 mm. Angular fitting is less reliable due to the limited angular acceptance of the collector, and thus avoided. An IDL-based code is responsible for taking in contour data and fitting a Gaussian

function to the weighted distribution (separately for both radial and angular considerations). [13] By default, all data in the plane is used for fitting.

To find the weighted radial fit, the IDL routine will take in beam data, overlay the expected (nominal) gyroradius, and then fit Gaussian centers to each angular slice. The routine then moves on to generate a finer interpolation of the grid before calculating the χ^2 values for each angular slice. Using these χ^2 to determine the relative weighting allows the routine to perform a weighted average over the angular slices of the radial profile. Once this is completed, a simple Gaussian average of the resulting weighted profile can be obtained in a straightforward manner, yielding the full width at half max (FWHM) of the distribution. Typical FWHM values for our collected spot range from 0.25 cm^2 to 2.00 cm^2 depending on beam and plasma parameters.

Chapter 3
Turbulent Transport of Energetic Ions in Electromagnetic Turbulence Generated via Magnetic Flux Rope

3.1 Experimental Setup

3.1.1 Experimental Overview and Nominal Parameters

This experiment is performed in the upgraded LAPD at UCLA. Background magnetic field in the axial direction is generated by current-carrying coils and can be varied up to 3.5 kG; the background magnetic field chosen for this experiment was 700 G. In the absence of flux ropes, background plasma parameters during the active phase of a 4 kA/60 V discharge are measured by interferometer and Langmuir probe. The background electron is found to be roughly 3 eV; the background ion temperature is expected to be around 1 eV, but has not been directly measured. The locations of the ion gun, ion collector, and flux rope hardware are shown schematically in Figure 3.1.1. Further information on ion beam parameters is shown in the table in Table 3.1.2.

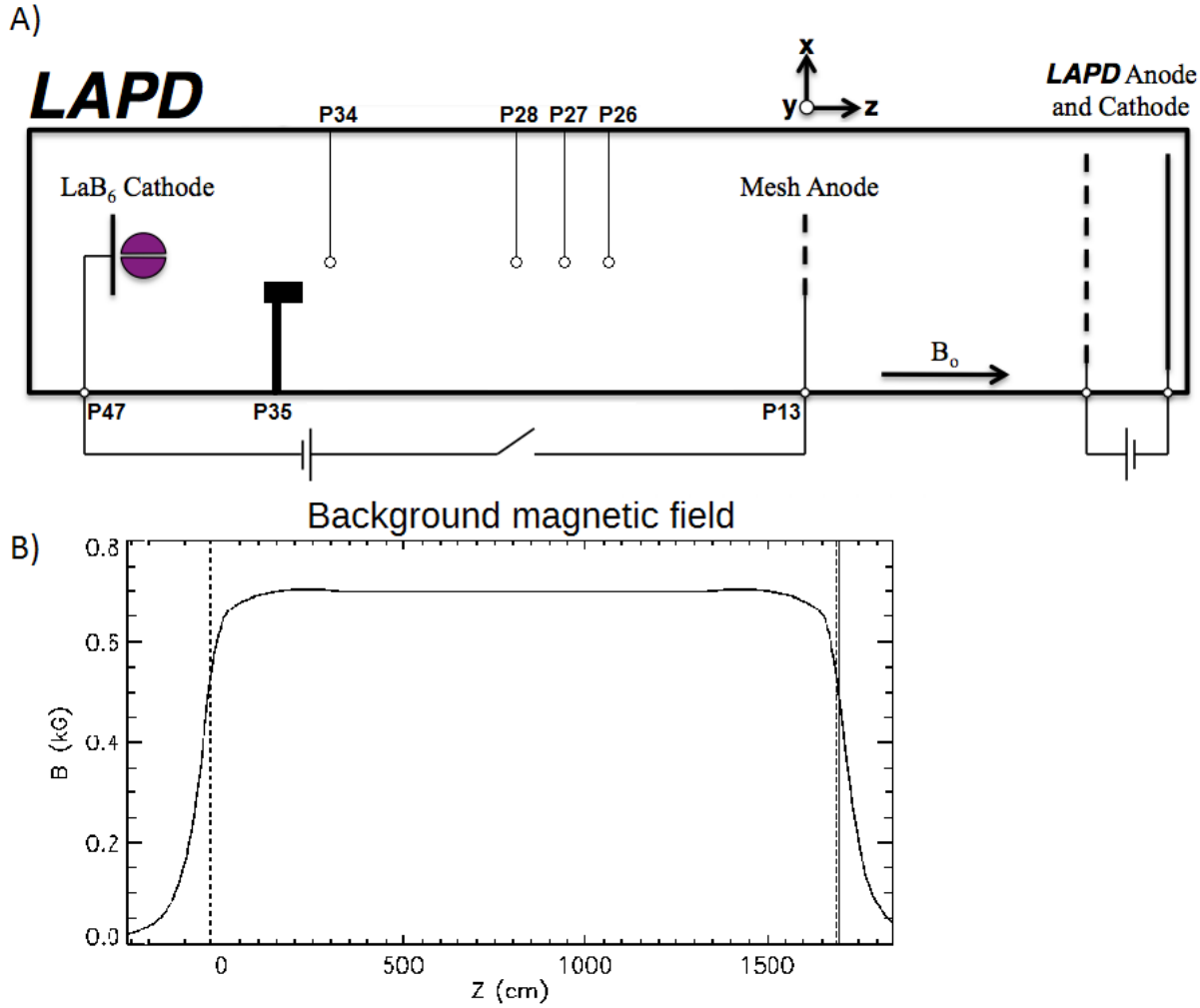

Figure 3.1.1 Experimental setup in the LAPD. (a) Schematic cross section of LAPD setup. The ion gun is shown at Port 35, with b-dot probes (Port 26 fixed, port 27 moving) and triple probes (Port 28 fixed, port 34 moving). (b) magnetic field profile generated from the current-carrying coils, 5 cm off the magnetic axis.

Number of Turns	1000 eV			700 eV			500 eV		
	TPP	ρ (cm)	χ (deg)	TPP	ρ (cm)	χ (deg)	TPP	ρ (cm)	χ (deg)
1	1/2	13.96	53.9	1/2	10.26	45.3			
2	1/2	13.96	53.9	1/2	10.26	45.3	1/1	11.10	65.4
3	3/7	12.55	46.6				3/4	10.16	56.3
4	4/9	12.93	48.5						
5				5/9	11.18	50.7			

Table 3.1.2 Table of nominal operating values for the ion beam at a given beam energy (see section 2.3 for more information on source operation). Turns per ports, or TPP, represents the number of gyroorbits performed per LAPD port. ρ represents the nominal fast ion gyroradius while χ denotes the fast ion pitch angle with respect to the background field.

An ion gun with attached industrial-grade Lithium ion source (see Section 2.3 for more detailed information) is interfaced with the LAPD at rectangular port 35 on the West side of the LAPD, as shown above in Figure 3.1.1. The ion gun is calibrated by inserting the head of the ion gun into the main LAPD chamber until the 5 mm aperture (illuminated by thermal emission of an enclosed Lithium source) is observed to be centered on the magnetic axis. Upon calibration, the ion gun can be rotated to various pitch angles with respect to the magnetic axis in order to generate helical fast ion trajectories that complete a known number of orbits over a certain distance. The helical trajectory can be treated as a superposition of azimuthal gyro-orbiting and axial propagation down the LAPD. The 5mm aperture in front of the ion gun's biased grids is responsible for the low-divergence properties of the emergent beam (±3 degrees angular FWHM), with the energy divergence (on the order of ±5 eV, as measured by FWHM fitting to the observed energy distribution) dictated by the biasing voltages applied to the grid in front of the Lithium ion source. Beam energy in this experiment is varied from 500 eV to 1000 eV. Typical test beam current densities are observed to be on the order of ~100 $\mu A/cm^2$. Nominal beam distribution is approximately Gaussian over a range of 2 cm, with a peak current density of roughly 200 μA.

Nominally, probes are interfaced with the LAPD from the East side of the device. Beam collection via fast ion collecting probes has shown to be problematic when immersed in the flux rope's active region, as shown in the comparison between collectors inserted from each side of the LAPD (Figure 3.1.3). Spurious electrical noise, attributable to the large power associated with the flux rope hardware, is responsible for compromising the beam signal. The active flux rope region is primarily concentrated within a radius of ~6cm about the magnetic axis. The East-inserted probe must be immersed in this region to collect ion beam data. Thus, in order to

maximize the signal-to-noise ratio, the probe shaft must be interfaced with the LAPD through the West-facing ports of the LAPD.

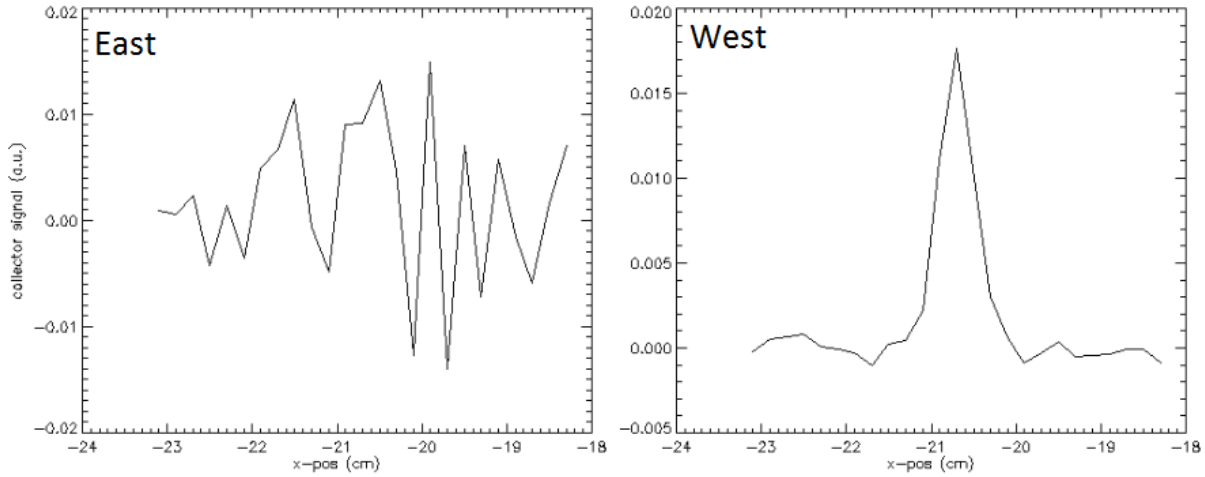

Figure 3.1.3 Noise trace comparison in A.U. For fast ion collector inserted into the LAPD from both sides. The recollected beam signal is lost in electrical noise when inserted from the East. Flux rope cathode nominally discharges 170 A at 160 V over a 4 ms period during the active phase of the primary LAPD discharge phase.

Basic collector operation involves acquiring data once every second during the discharge period (for more information, see Section 2.3.2). For this experiment, the collector is aligned to the same angle as the ion gun upon insertion into the LAPD. The collector is situated in one of five axial positions along the LAPD, as dictated by the current ion beam orbit being studied, recapturing the ion beam between one and four gyro-orbits downstream.

The magnetic flux ropes are generated near the center of the magnetic axis by the flux rope cathode hardware (located at port 47) and an anode initially located at port 13 (described in Section 2.4.1), shown above in Figure 3.1.1. While the flux rope cathode remains stationary for the duration of our experiment, the flux rope anode can be moved downstream to port 41, closer to the flux rope cathode, beyond the fast ion gun as a means of reducing turbulence experienced by test ions.

3.1.2 Flux Rope Characteristics

Perturbations in the background plasma are observed as a result of the flux ropes. The active region is observed to have an increased electron density and density gradient near the magnetic axis, density fluctuations, as well as the generation of a perpendicular magnetic field.

Magnetic flux ropes generated via secondary cathode/anode have been studied in the LAPD with the help of B-dot probes and Langmuir triple and swept probes. B-dot probes placed within the active flux rope region show appreciable increase to perpendicular magnetic field due to the presence of flux ropes. Triple Langmuir probes separated by a distance of 6 ports (1.9 meters) are used to diagnose the structure of the density and floating potential (see section 2.5 for more details).

FFTs of B-dot data can be used to help determine what the flux rope mode structure looks like, if it has any. As shown below in figure 3.1.4, the FFT obtained from B-dot data shows clear mode at ~7 kHz, corresponding to the kink mode of the flux rope. Higher harmonics are also observed. Higher frequency, wider band electrical noise attributable to the flux rope hardware is also observed.

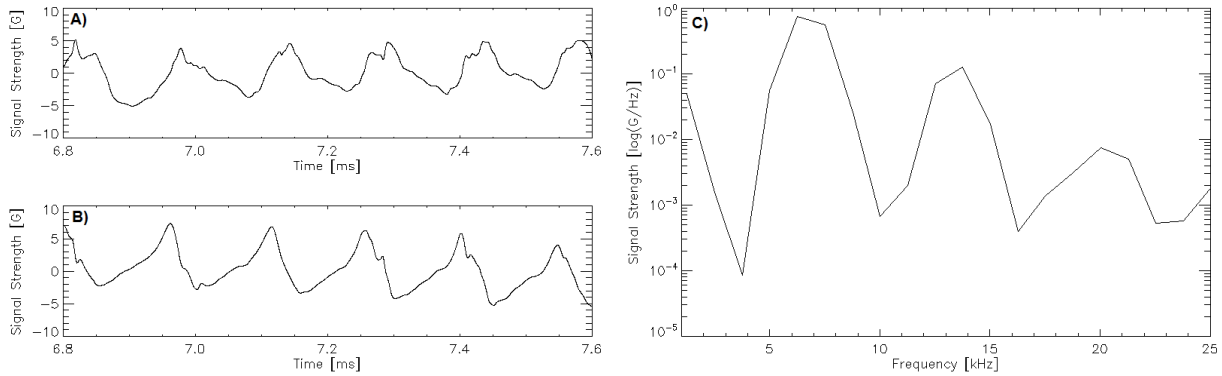

Figure 3.1.4 Magnetic field time traces of perpendicular components A) B_x and B) B_y in the active region (x = -1.2 cm, y = 1.8 cm) during the flux rope discharge period. C) Fast Fourier transform of the y-component of the magnetic field during this time period. B-dot probes are positioned at ports 26 (reference) and 27 (moving). Maximum observed magnetic field strength is 7.4 G for a flux rope discharge of 170 A at 160 V.

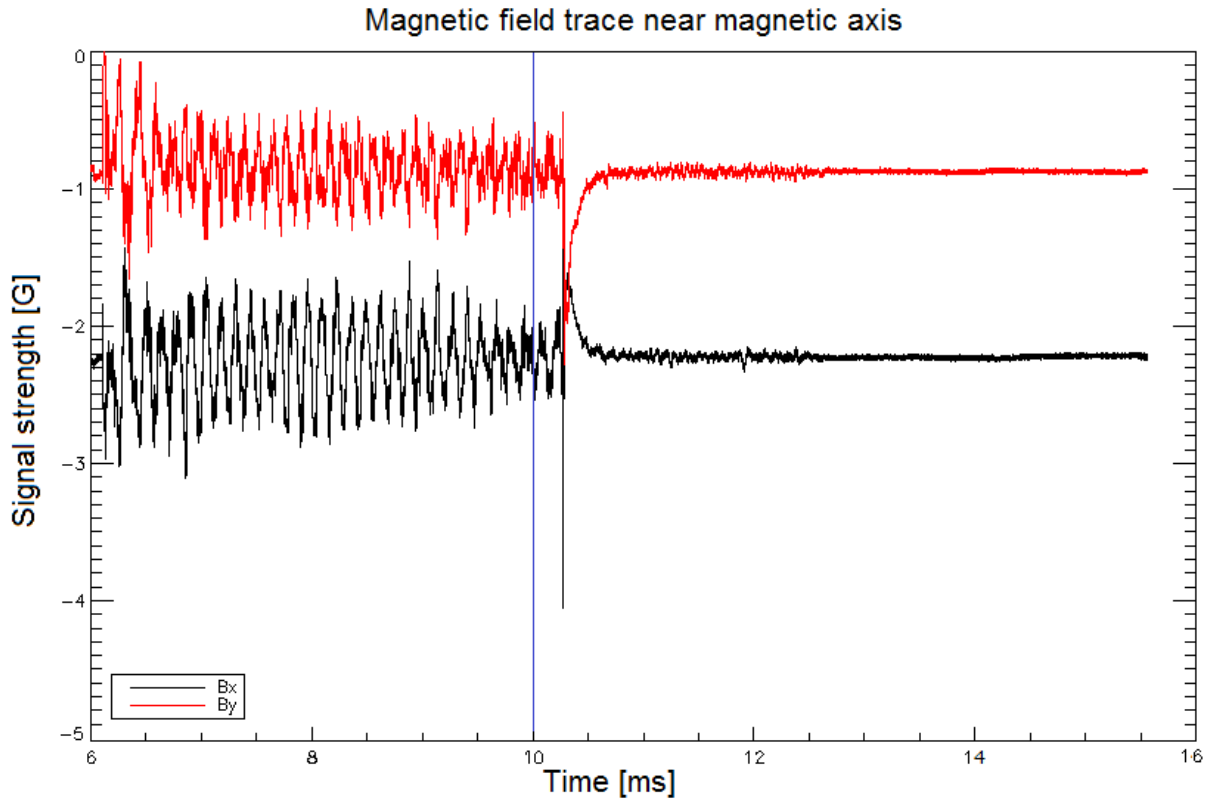

Figure 3.1.5 A time trace shows the oscillations observed in Bx and By data taken via b-dot probe near the magnetic axis (x = 7.5 cm, y = 0 cm) during a nominal flux rope discharge event (170 A/160 V), seen from approximately 6-10 ms. The data is observed to have DC offsets related to hardware interfaced with the data acquisition system (DAQ). Flux rope turn-off time is shown with a vertical blue line.

Using the approach outlined in Section 2.5.2, B-dot data taken over a 2D plane can be used to reconstruct the background field when the flux ropes are on. The signal obtained via B-dot probe is the time-derivative of the magnetic field for each coil, yielding derivatives of B_x, B_y, and B_z. The magnetic field can be obtained by an integration routine: After defining a calibration function and subtracting background signal, B-dot time traces are transformed into frequency space. Upon application of the calibration function, the signal is numerically integrated. Finally, the fluctuating field is obtained by inverting the transformation. Representative time traces at a single spatial location are shown above in Figure 3.1.5; magnetic fluctuations at this location are observed to be on the order of a few G peak-to-peak. As shown in figure 3.1.6, the magnetic field structure is modified appreciably from the flux rope off state. The

maximum perpendicular field strength is observed to be 7.4 G. The fluctuations occur when the flux rope currents are energized, principally in the perpendicular direction, and have spectral components primarily between ~5-100 kHz.

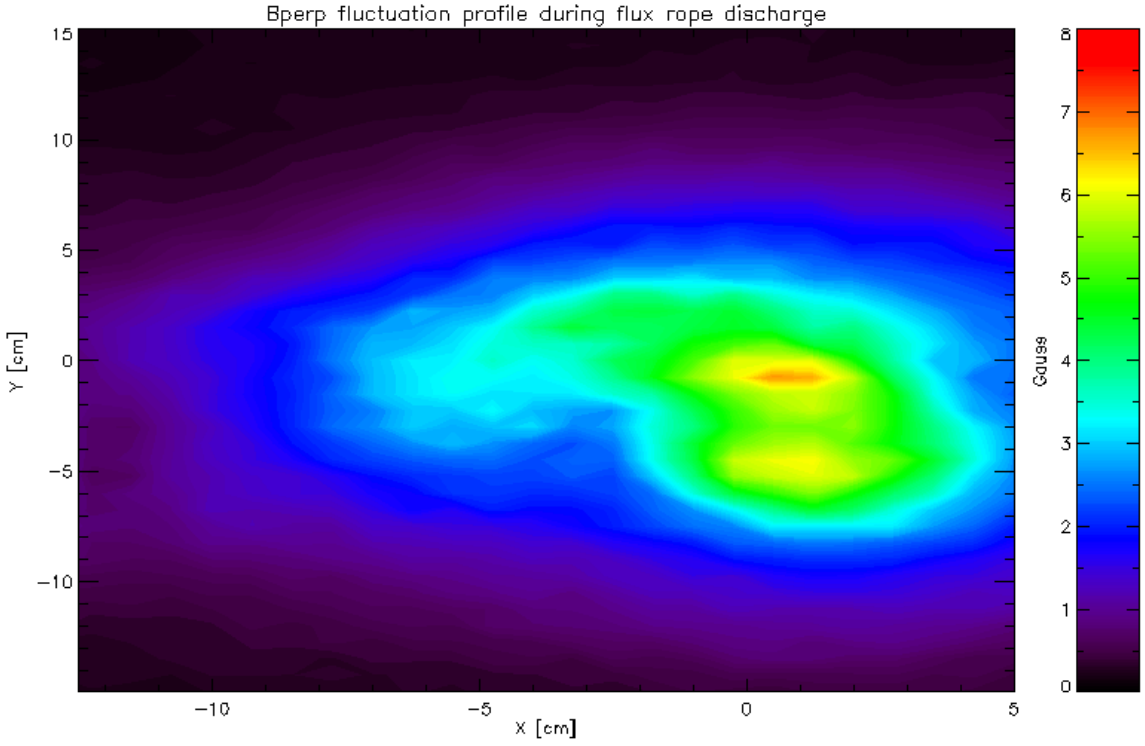

Figure 3.1.6 Magnetic field plane for a 160 V flux rope discharge, observed to peak at just over 7 G in the active region.

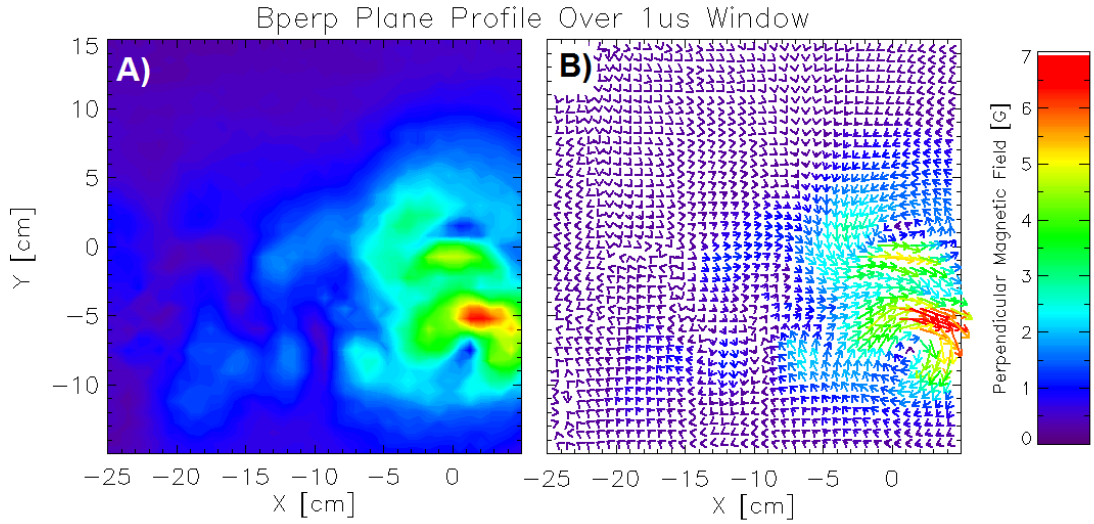

Figure 3.1.7 A) Magnitude and B) vector profiles of the perpendicular magnetic field produced by the flux ropes taken via B-dot probe at port 27. Strong activity is observed near the magnetic axis. Peak field strength is ~7 G.

A complementary analysis is carried out for the background electric field and electrostatic fluctuations. Triple Langmuir probes separated by a distance of 6 ports (1.9 meters) are used to diagnose the structure of the density and floating potential fluctuations. Field data are obtained with a combination of triple probe plane scan and swept probe line scans. Field data are temporally aligned via cross correlation with a reference signal. Upon interpolation to a finer grid, the electric potential profile is obtained. From this profile, both the background field as well as fluctuations about the background are determined. The maximum electric field strength is observed to be ~862.4 V/m in the active region. The background field is expected to deflect the beam centroid without appreciably increasing spreading. Shear between the fast ion beam and the background electrostatic field can lead to additional spreading. This interaction depends on the scale length of the beam spot size, which is on the order of a centimeter. As such, this effect is excluded from further consideration as a result of the negligible size of this effect.

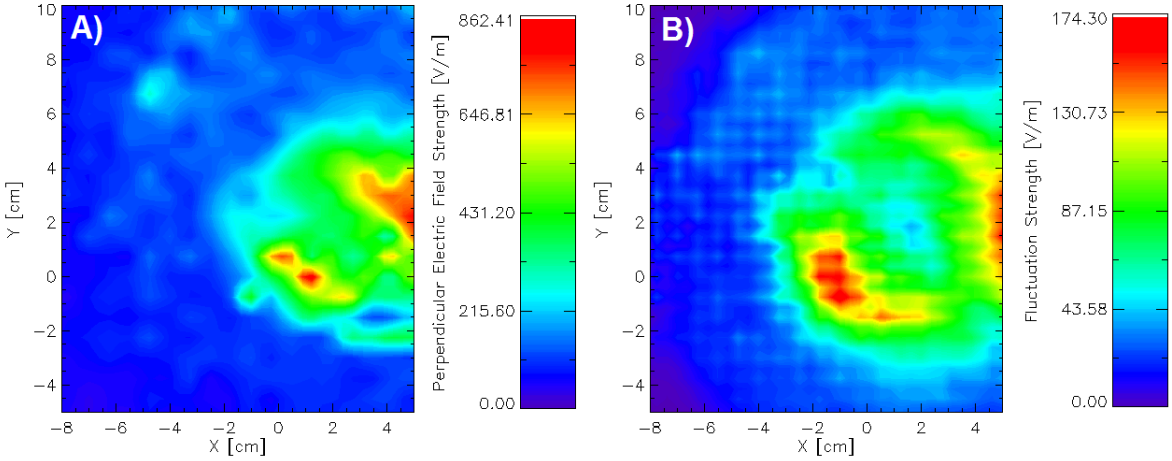

Figure 3.1.8 A) Perpendicular electric field profile at t = 7.1 microseconds and B) fluctuation profile produced by the flux ropes at port 34. Strong activity is observed near the magnetic axis. Peak field strength is ~860 V/m.

The temperature of different portions of the electron population is obtained via I-V trace. The temperature data can be further extended to 1-dimensional and 2-dimensional profiles from swept line and plane data acquired at the LAPD. Nominal fitting of the temperature in the bulk(/tail) electron distribution is performed by finding the exponential deviation from ISAT(/ESAT) in the I-V curve data, as discussed previously in Section 2.5.1.2. The resulting temperature profiles show an increase in electron temperature near the magnetic axis when the flux ropes are energized. The two flux rope channels are located in this region, each centered 2.5 cm off-axis, with radii of 1.5 cm.

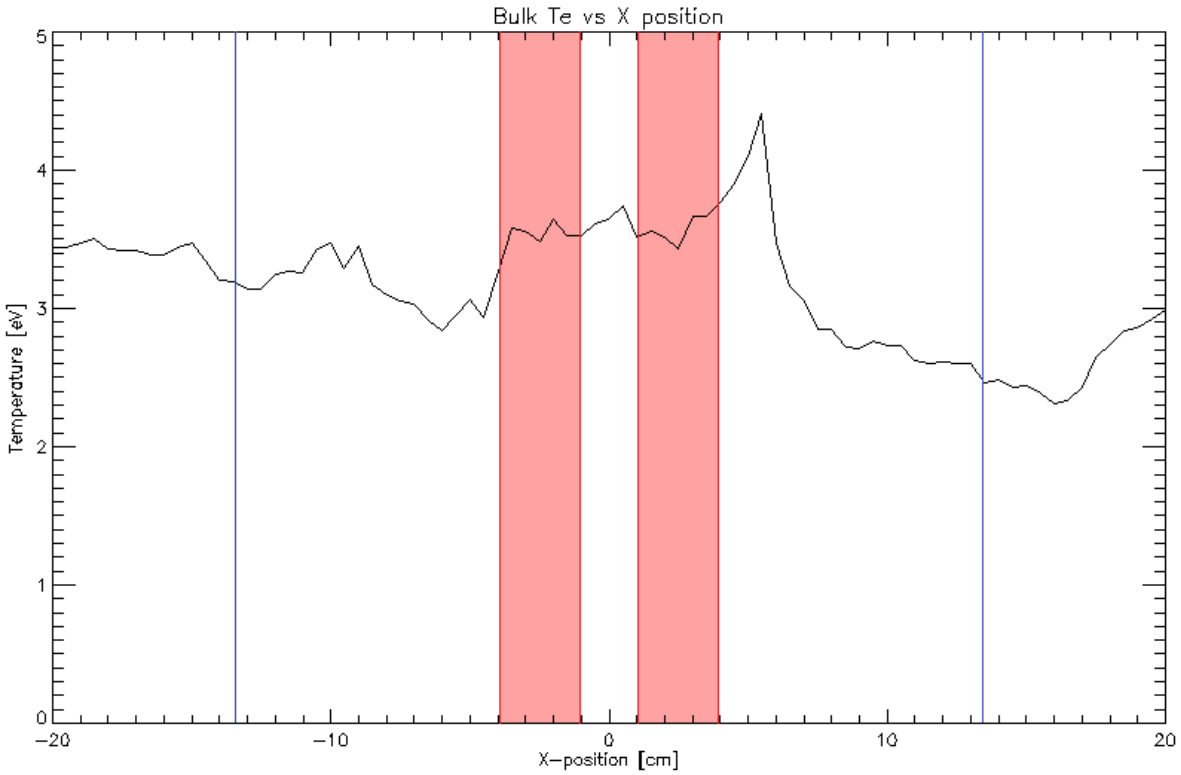

Figure 3.1.9 Bulk electron temperature profile for a flux rope discharge at 160V. The edge of the flux rope hardware is shown with solid blue lines, while the location of the nominal locations of the two flux ropes on the mask are indicated in red.

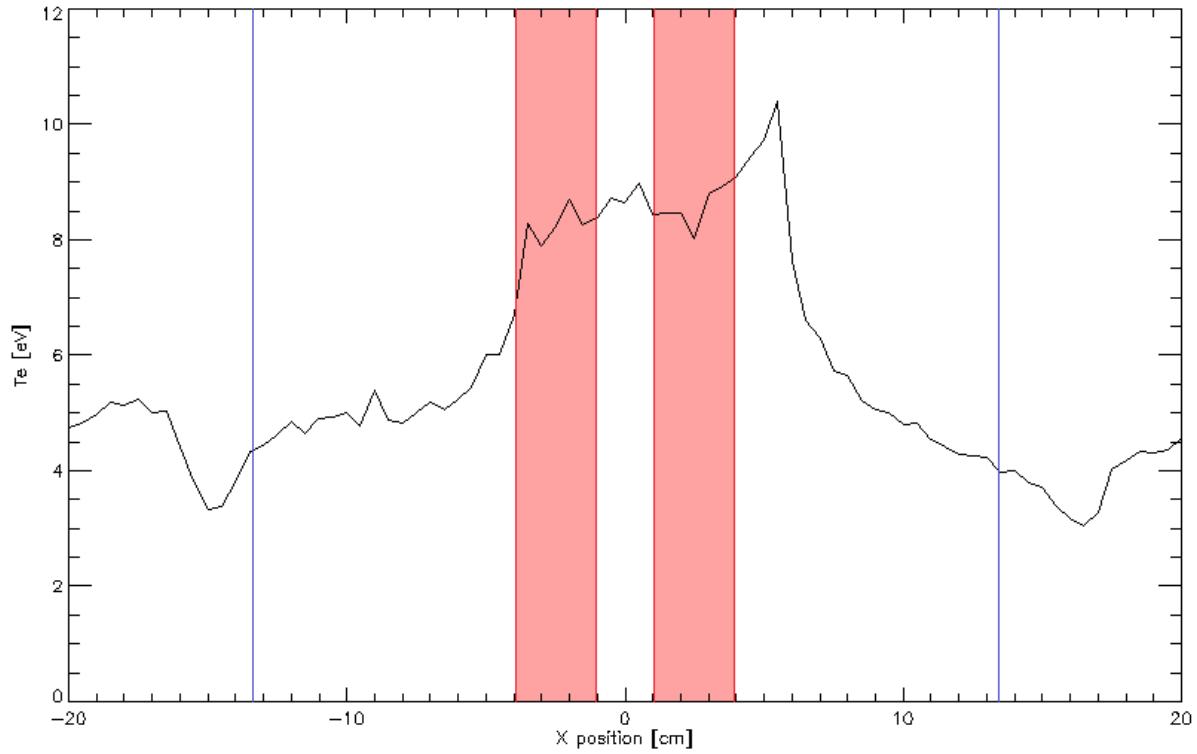

Figure 3.1.10 Tail electron temperature profile for a flux rope discharge at 160V.

Electron temperatures fit in the tail region can be falsely increased by the presence of noise. Care was taken in processing these results to minimize the influence of spurious electrical noise on the exponential fits to the data. The data was processed on a shot-by-shot basis, wherein signals that were significantly elevated above the mean were excluded.

The observed increase in the bulk temperature may be attributable to the primary LAPD cathode/anode discharge; the axial temperature profile in the LAPD will nominally have an increase near the magnetic axis. For comparison, previous data has observed a ~2 eV increase in electron temperature at the magnetic axis w.r.t. background levels. [14] This suggests the bulk electrons are unmodified during the flux rope discharge.

3.1.3 Anode-Shifted Characteristics

A complementary analysis can be carried out for the case in which the flux rope anode is moved

as described in section 3.1.1. Despite moving the anode downstream to port 41, an increase in electron temperature is observed in the anode-shifted case (Figure 3.1.11).

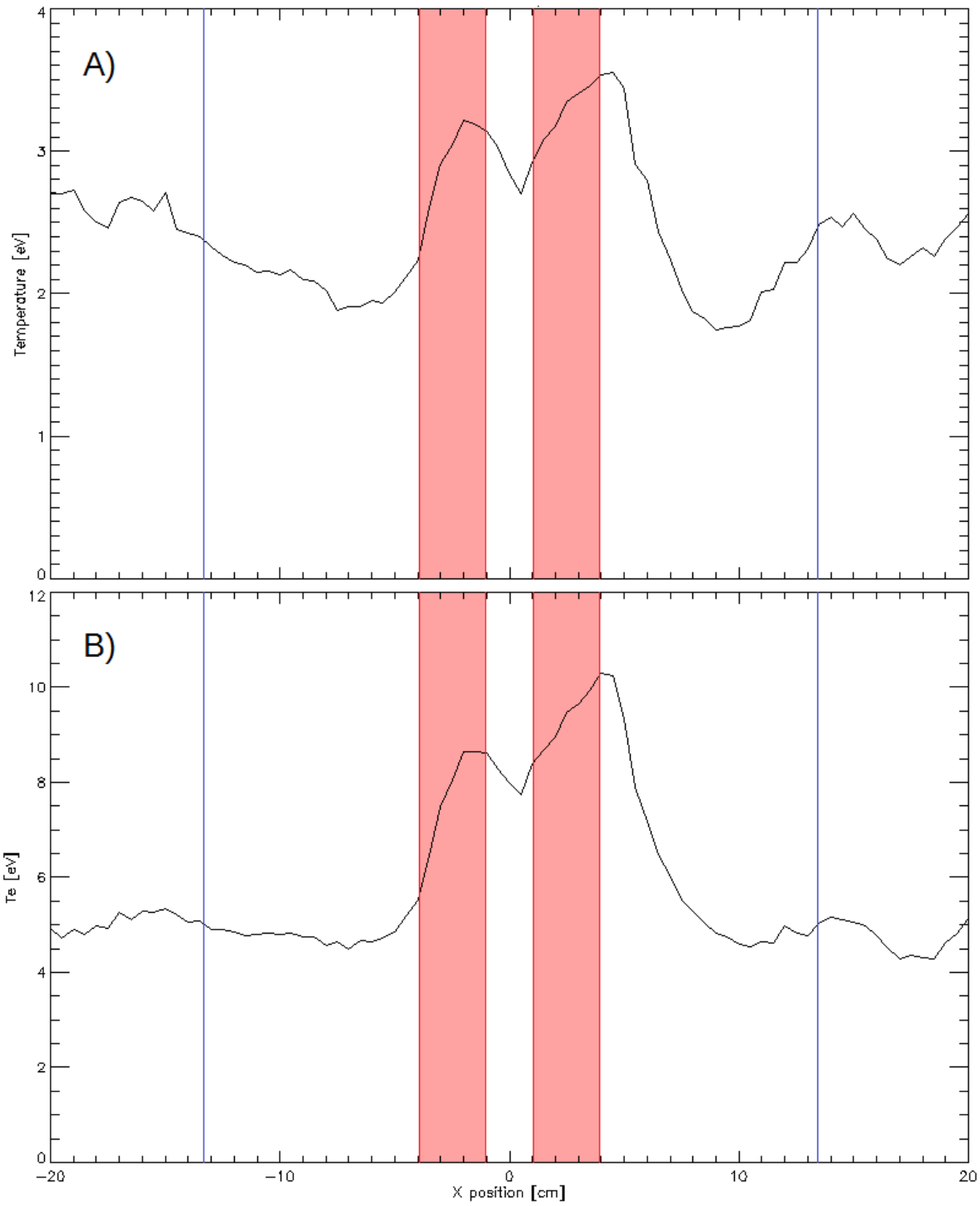

Figure 3.1.11 Bulk (a) and tail (b) electron temperature profiles during flux rope discharge at 160 V while anode shifted to port 41.

As before, the observed increase in the bulk temperature is consistent with past observations of the primary LAPD cathode/anode discharge. The tail temperature, however, still appears to be elevated above background levels even after the flux ropes have discharged. The elevated temperature profile may be attributable to the time associated with dissipation of the current channel. The current channel takes time to travel downstream, suggesting portions of the rope may still be discharging.

Further, it is necessary to understand how the magnetic field profile changes after the flux rope discharge. Unfortunately, B-dot data taken over a 2D plane did not continue beyond the flux rope discharge, making it impossible to generate a 2D profile. B-dot time traces obtained by fixed probe, however, illustrate that the fluctuating amplitude decays to zero within ~300 μs of terminating the discharge (see Figure 3.1.5).

3.1.4 Signal-to-Noise Ratio Modeling

As briefly discussed in section 3.1.1, noise generated by the flux rope hardware can be rather significant. A careful treatment of how the noise interacts with FWHM fitting of ion beam data is thus warranted. High-intensity spurious noise is observed to be present across all data collected during flux rope discharge periods.

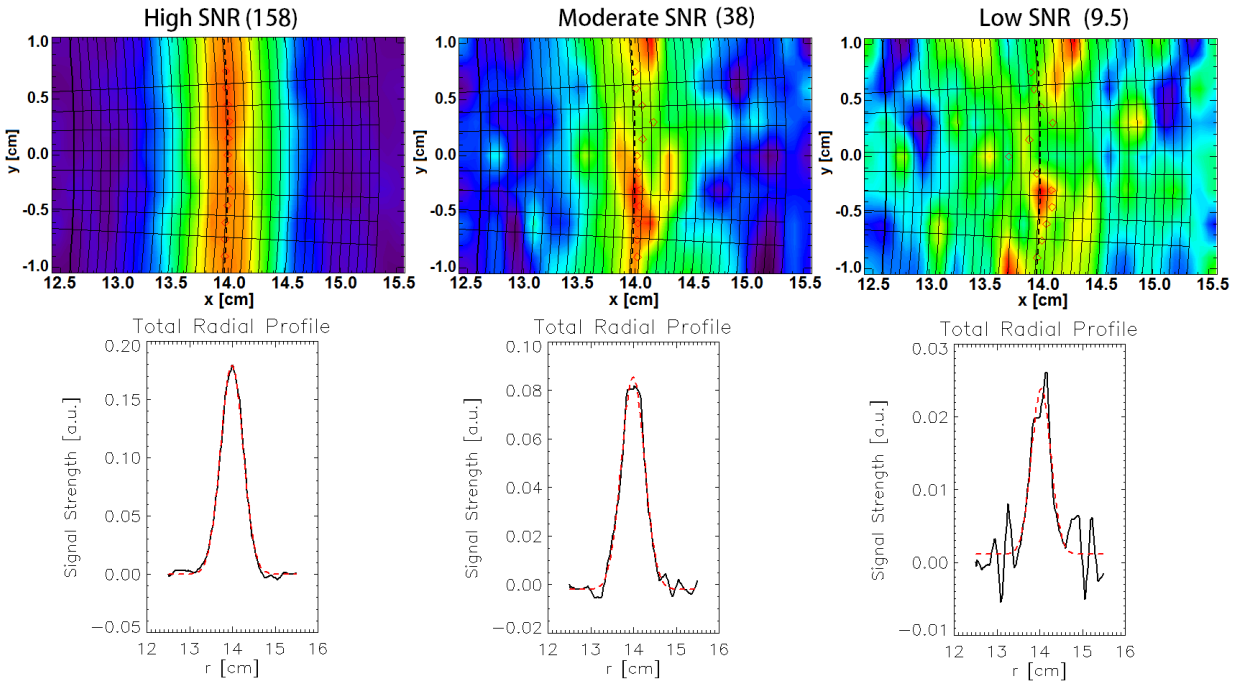

Figure 3.1.12 Signal-to-Noise ratio (SNR) comparison for an initially-identical array of model ion beam data. Higher intensity normally-distributed noise is added as you move to the right. The dashed line is the radial fit.

As shown above in figure 3.1.12, the average FWHM is observed to increase as the amount of noise in the data increases. The influence of the noise on the data is most prominent at low SNR values, causing significant errors in the resulting FWHM fit. All three sample FWHM in figure 3.1.12 are initially identical. The beam data is then convoluted with noise of a given strength. The introduction of additional noise is observed to lead to notable discrepancies in the resulting spot fit. The same process is carried out for a large sampling of FWHM data convoluted with noise.

Given the large amount of data being handled, modeling and fitting via IDL is employed. To start, a routine is created that will take a desired radial FWHM value as input and output a two dimensional array of ion beam data of the given size. This routine is then further modified by allowing the program to add random noise at a known amplitude. This allows for the creation of a large number of model beam profiles to study; ensembles of 1000 ion beam data grids with spatial size and resolution similar to LAPD data are generated with a random normal noise

distribution at a known strength. These spots are then individually fit before having the results of the ensemble analyzed. The noise strength is then iterated and the process repeats again until the program has completed the sweep through "noise intensity" space. The entire process as described above is applicable to a single FWHM ion beam. In order to find out how larger (or smaller) nominally-sized beams respond to noise, the process is then repeated across a range of radial size. See Appendix A for more information on the source files used in this chapter.

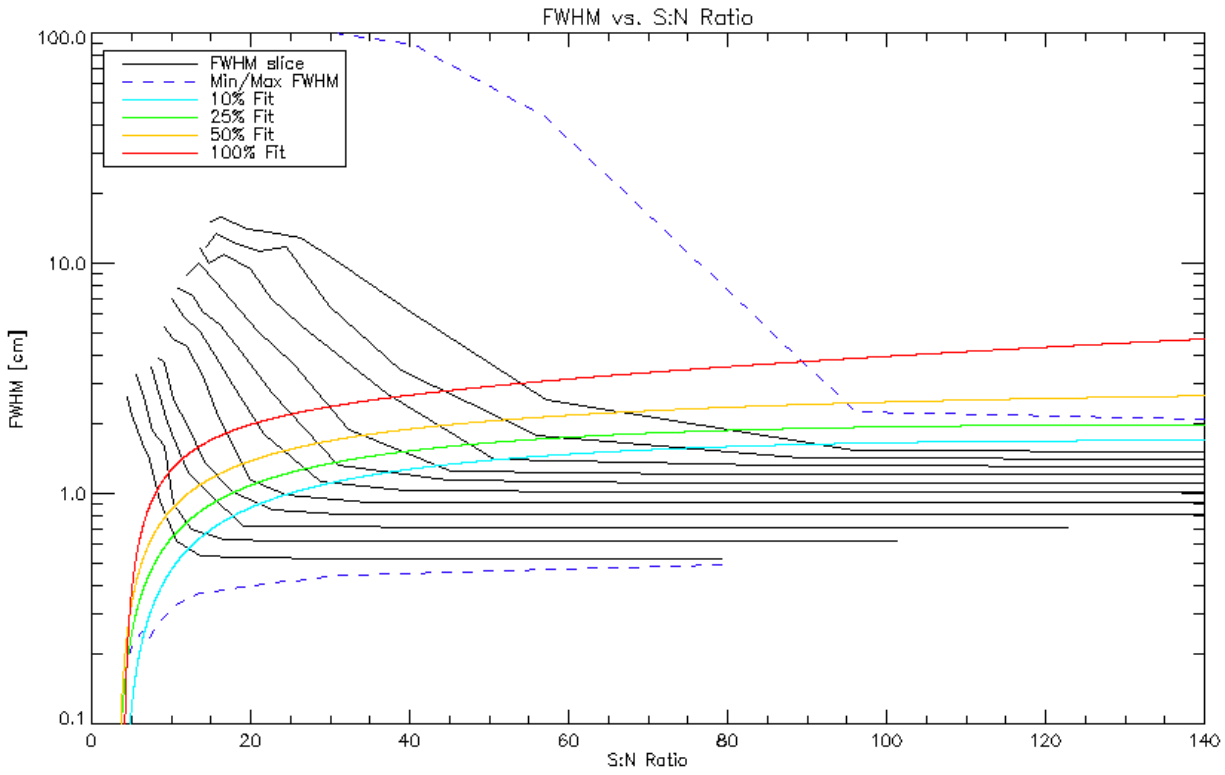

Figure 3.1.13 Calculated effect of different signal-to-noise ratios on the fit radial FWHM of the beam spot. Solid black lines represent the mean FWHM obtained at a given noise value. Solid, colored curves represent best-fit polynomial solutions to the given error values. The dashed blue lines represent maximum and minimum FWHM values obtained via fitting.

Similar to the results discussed above for Figure 3.1.12, the FWHM fitting becomes less reliable in the presence of increased noise (at low SNR). The flux ropes generate additional noise in the collector signal. This raises the question: "Is the additional broadening measured during the flux rope discharge due to enhanced transport or due to an instrumental effect?" To address this

question, signal-to-noise ratio (SNR) modeling has been developed to quantify the potentially significant errors in the resulting FWHM fit. An ensemble of 1,000 model beam spots are created for each nominal beam size, ranging from 0.5 cm to 1.5 cm. The model data is then convolved with random noise at a known amplitude. These spots are then individually fit before having the results of the ensemble analyzed. The noise strength is then iterated and the process repeated until the program has completed the sweep through "noise intensity" space, yielding the noise map (Figure 3.1.13). Colored curves represent expected measured FWHM at a given noise level. The curves are obtained by taking polynomial fits of 11 points in FWHM-SNR space. Further, while the mean FWHM is observed to increase, some data is observed to undershoot the nominal fit value (represented as the lower, dashed blue line). The maximum and minimum measured FWHM become increasingly disparate as the noise is increased. In conclusion, increases in outside noise tend to cause overestimates in the measured FWHM of an ion beam. As such, the contributions from noise must be treated carefully.

3.2 Experimental Results

3.2.1 Observed Radial Beam Broadening in the Presence of Flux Ropes

A nominal comparison of the ion beam signal collected for the "flux rope on" case against the background "flux rope off" case is obtained by processing collected data at different times during the same run. "Flux rope on" beam data is acquired from a time window during the 4 ms "on" period in the LAPD. The ion beam data during the "flux rope off" time are obtained prior to the flux rope discharge.

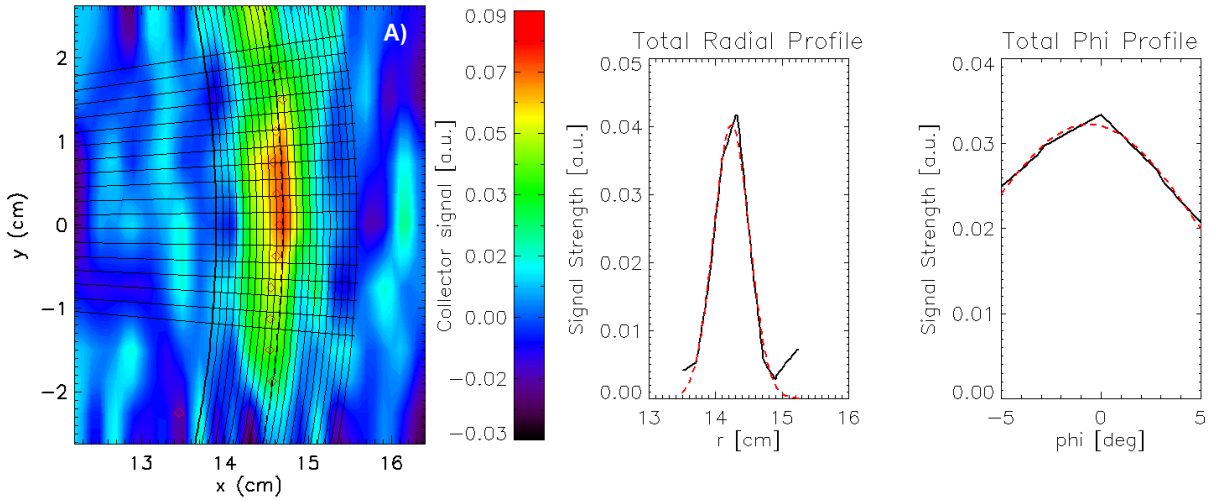

Figure 3.2.1 Sample gridded ion beam data obtained via fast ion collector. Data is fit in radial and angular directions by IDL-based fitting routine.

As shown above in Figure 3.2.1, quantitative fits to the data are obtained as outlined in Section 2.5.3. Fitting fast ion data from the period before the flux rope discharge can be directly compared to fits obtained for the "flux rope on" case, and reveals a notable increase in transport attributable to some mechanism of the flux rope discharge. For the case of a 1000eV fast ion beam collected four ports downstream, an observed change on the order of 0.3cm^2 is observed (as shown below in Figure 3.2.2). The signal-to-noise ratio for this condition is 23.9, which indicates that an increase in broadening due to noise alone is less than 10%. This represents a good-quality fit.

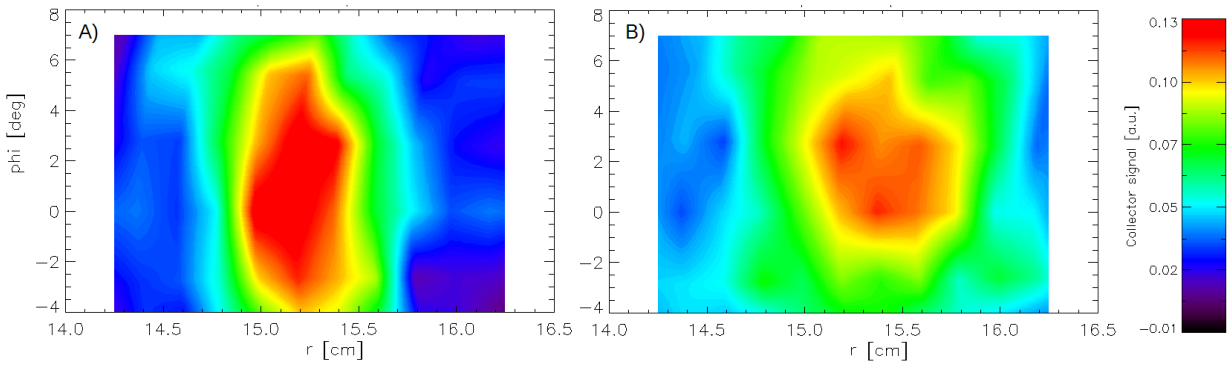

Figure 3.2.2 Comparison of ion beam signals collected for the "flux rope on" and "flux rope off" cases for a 1000

eV ion beam launched at a pitch angle of 53.9° w.r.t. the magnetic axis. The beam performs half a turn per LAPD port in a 700 G background field (with 13.9 cm gyroradius).

3.2.2 X-position Dependence of Radial Transport

While it is straightforward to set up the ion beam to travel though the perturbed region, it is not known a priori exactly how to maximize flux rope interaction. Thus a scan in X-space was performed. While the flux ropes pass through the magnetic axis (determined by the location of the cathode/anode hardware), the initial location of the ion beam can be readily changed.

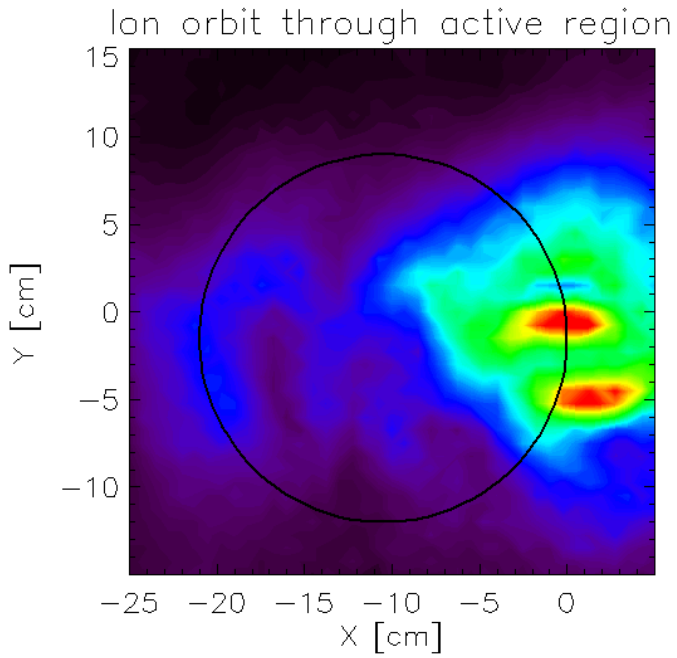

Figure 3.2.3 Schematic diagram of the ion beam alignment with the flux rope region, from the perspective of a 2D plane at some axial distance along the LAPD.

Fast ions with the same parameters as above (1000 eV beam, 53.9° pitch, 13.9 cm gyroradius) are launched at different x-positions, starting from 2 gyroradii from the magnetic axis. Such a beam will transit directly through the magnetic axis as it propagates down the LAPD. After this data is obtained, the ion beam is shifted left/right in increments of 2.5 cm. Given the physical

size of the LAPD as well as the limited insertion length of the ion gun, only certain x-positions within the device are accessible.

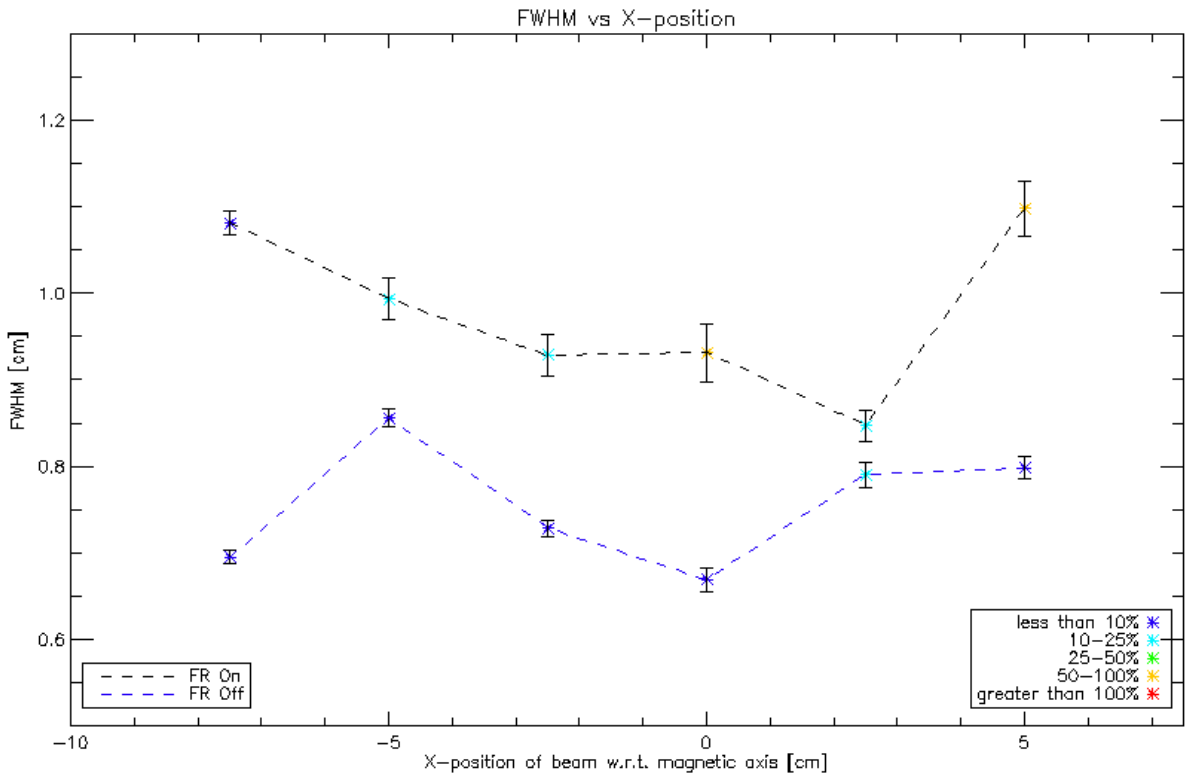

Figure 3.2.4 FWHM vs. X-position for ion beam data collected 4 ports downstream (port 31).

It is unknown a priori at which radial position the beam broadening due to flux ropes will be maximized. A line scan in the x-direction is performed (Figure 3.2.4) in order to determine the optimal alignment of the fast ion beam hardware. This process involves launching fast ions from varying x-positions, corresponding to different orbits through the active region near the magnetic axis. Upon collection, gridded fast ion data are fit as previously discussed. While the beam is broadened at all positions, no maximum is observed. The largest increase in beam size is observed for orbits farthest from the magnetic axis. Calculation of signal-to-noise values confirms that the data are well-fit despite increased noise that is observed in the flux rope "on" case. Error bars are included, and represent the error in weighted FWHM fitting performed via

IDL routine discussed in Section 2.5.3. As demonstrated earlier, noise in the data can contribute to errors in fitting and must be treated carefully. Signal-to-noise values have been included in the figure above, and demonstrate that most of the data is well-fit. Flux rope "on" beam data is observed to be noisier than its flux rope "off" counterpart. . The right edge (+5 cm) is chosen as the nominal position for beam data acquisition, as it is readily accessible to our hardware and shows a clear signal.

3.2.3 Energy Dependence of Radial Transport

Following the procedure outlined above to compare beam data for flux rope on/off cases, beam data is obtained at 500 eV, 700 eV, and 1000 eV at various axial locations along the LAPD (see Figure 3.1.2 for relevant beam parameters). In order to get quality beam signals, beams of varying energies were recaptured between 2 and 4 ports downstream.

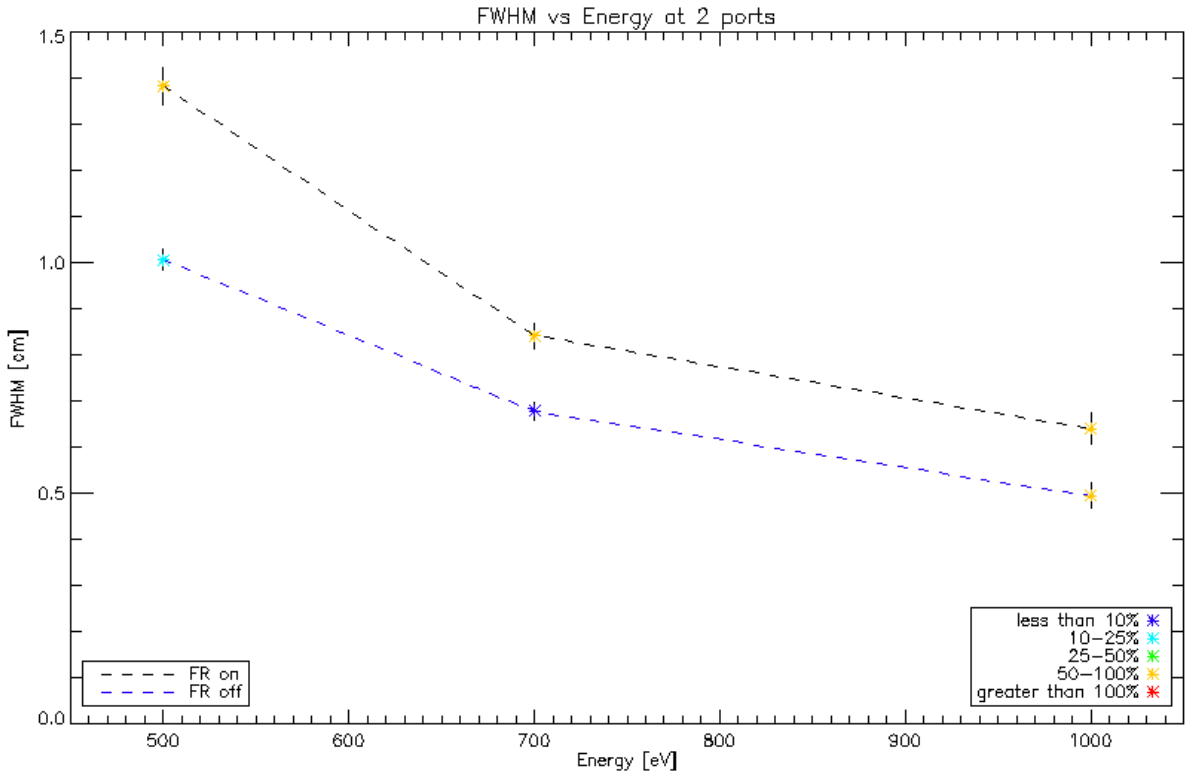

Figure 3.2.5 FWHM vs Energy for ion beams collected two ports from ion source.

As shown in Figure 3.2.5 above, clear spreading is observed at all fast ion energies as a result of turning on the flux rope hardware. Given the potential for contaminating our signal with noise, it is prudent to consider how strong an effect noise has on these results. Two points show strong confidence levels, while the remaining four fall in the yellow regime, representing 50-100% potential influence of noise. The yellow regime, generally, represents data that begins to become problematic. Manual inspection of the quality of the fits with respect to noise shows noise to be at tolerable levels for all data points.

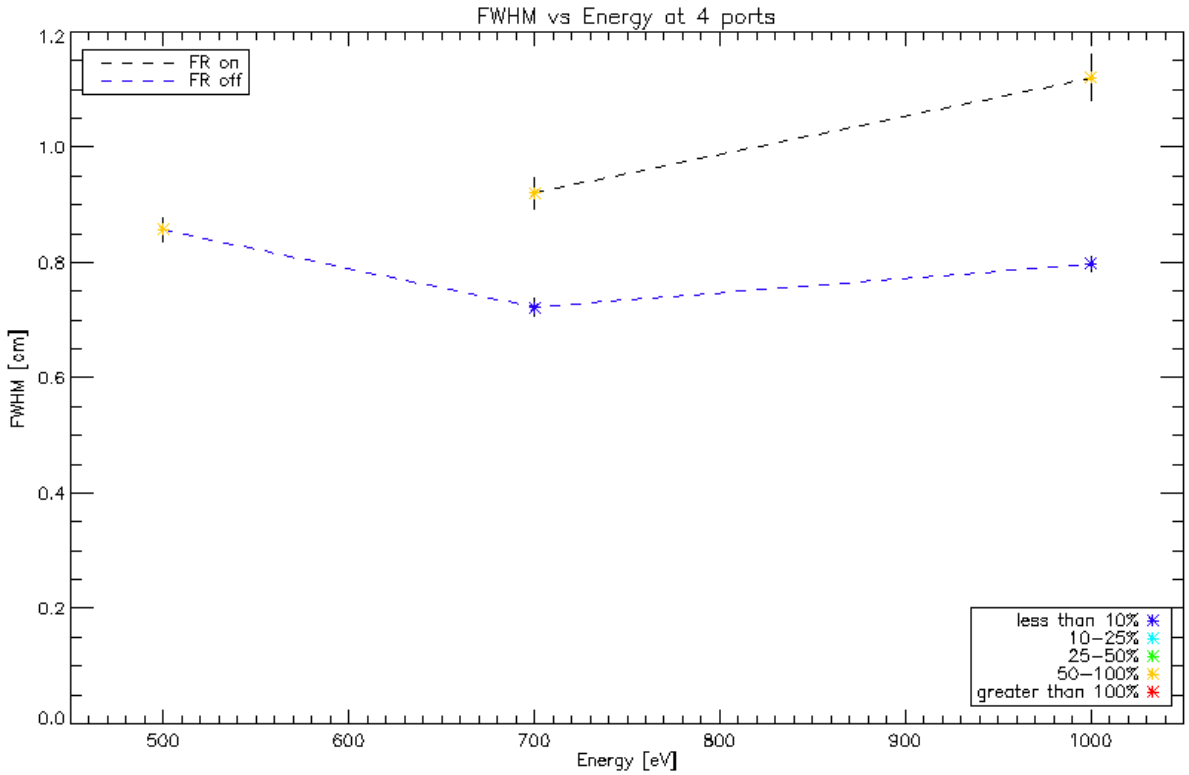

Figure 3.2.6 FWHM vs Energy for ion beams collected four ports from ion source.

An energy scan at 4 ports away reveals a similar trend. An increase in beam size is observed across all energies at this distance as well, including for the 500 eV "flux rope on" case that has been omitted from the plot. An issue presents itself when attempting to fit this result – the signal to noise ratio drops appreciably, yielding an unreasonably-large fit value to the FWHM. A combination of weak initial signal and increase in flux rope-attributed noise led to a significantly

compromised signal in this case. With an observed FWHM fit of ~1.4 cm and a SNR of 16.5, this fit result is situated rather far into the 100%+ noise regime shown in Figure 3.1.13. Though the data clearly shows signs of enhanced spreading in the presence of flux ropes, a meaningful quantitative fit cannot be made (and should not be taken as a reliable data point).

3.2.4 Time Dependence of Radial Transport

As discussed earlier, the motion of the fast ions can be deconstructed into a gyro-orbitting component and an axially propagating component. The axial component, represented by nearly constant v_z, allows axial distance to stand as a proxy for fast ion transit time when captured at a known distance from the source. Thus, in order to probe the time dependence of the transport, we need to use an ion beam that is readily observable a few meters downstream from our ion gun. The 1000 eV ion beam case is particularly well-suited to these studies as a result of its strong signal strength as far away as 9 ports (just under 3 meters) from the ion source.

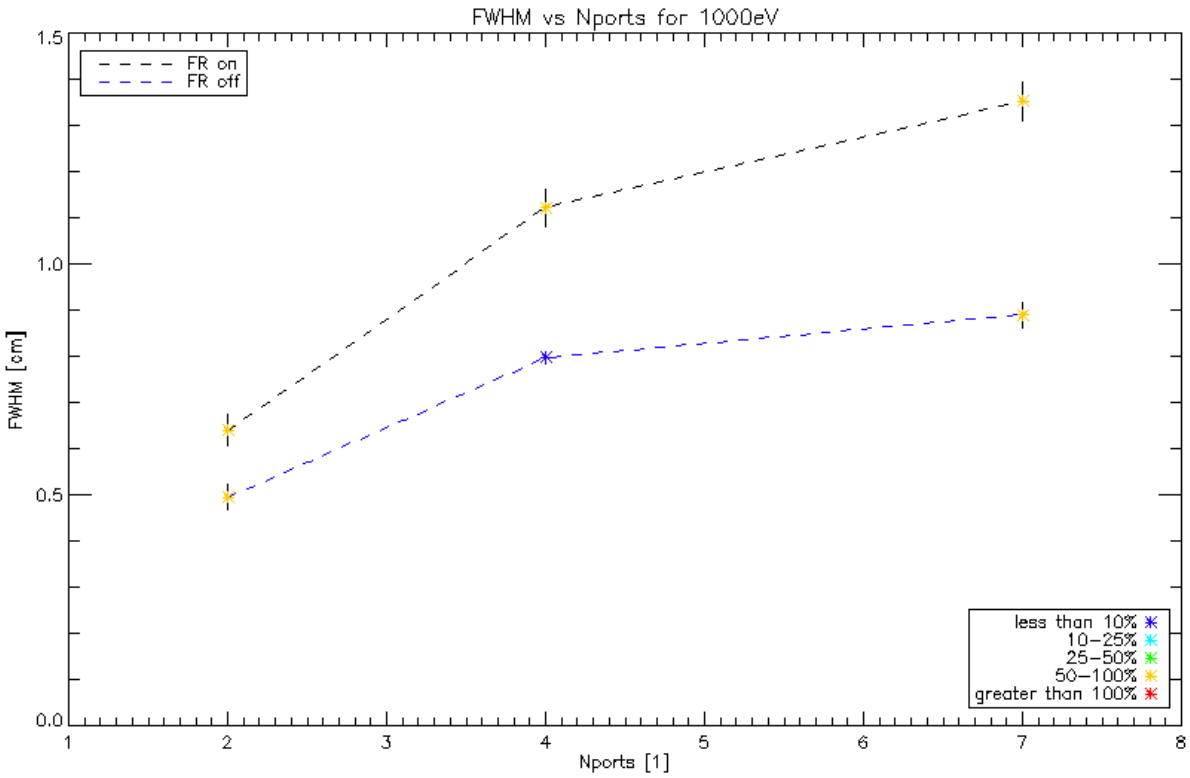

Figure 3.2.7 FWHM vs number of ports from ion source for a 1000 eV ion beam.

As shown above in Figure 3.2.7, clear broadening is observed when the flux ropes are turned on. Error for the 1000 eV FWHM fits is minimal, as represented by the included error bars. Signal-to-noise analysis shows the presence of some appreciable noise in five out of six of the cases. This is the result of the data being captured with a dying ion source producing weaker-than-expected ion emission currents. Inspection of the data confirms the fits are reliable despite the attenuated signals.

3.2.5 Anode-Shifted Ion Beam Data

Ion beam data can be collected after the flux rope anode is shifted to top rectangular port 41. This places the flux rope hardware (both cathode and anode) completely behind the fast ion gun and collector. The collection procedure is otherwise unmodified.

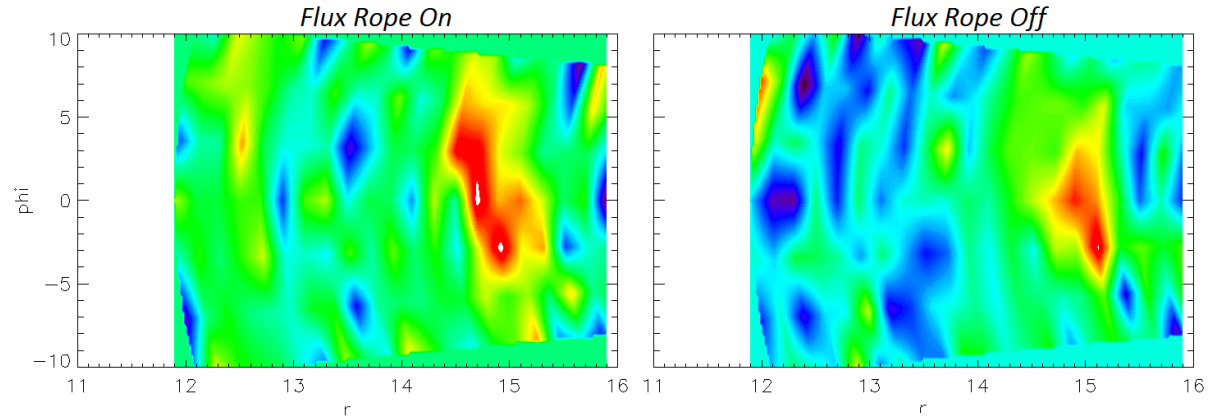

Figure 3.2.8 Interpolated beam profile for a 1000 eV beam captured four ports downstream from the source. Both fits represent poor-quality (noisy) FWHM fits, with SNR values of 6.72 (left) and 5.90 (right).

The first anode-shifted data set was collected for a 1000 eV ion beam captured 4 ports downstream. This data represents a fading Lithium ion source; the signal strength is weak as a result, and noise plays a significant role in any fitting attempts. This is further confirmed by finding the SNR values for this set of data, which are 6.72 and 5.90, respectively. Both values are particularly low, and represent a beam signal within the 50-100% error regime (red) in the SNR model shown previously in Section 3.1.4.

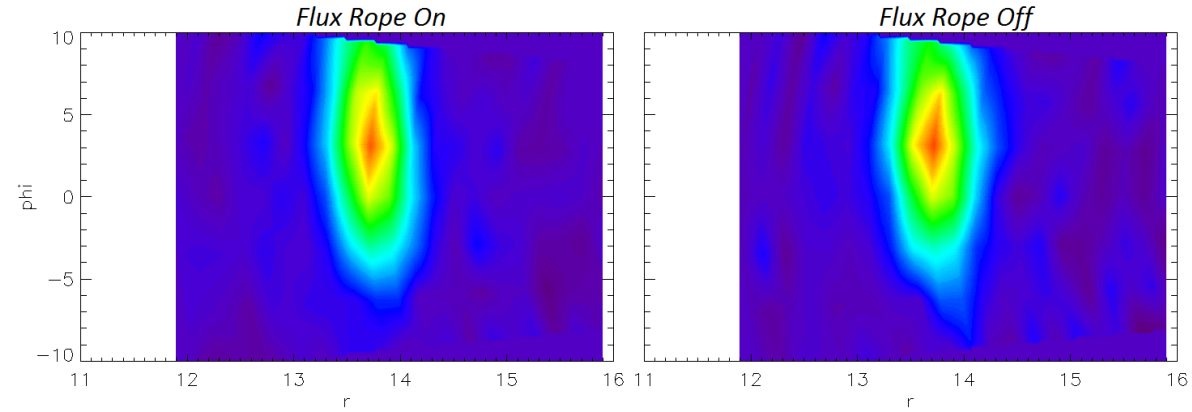

Figure 3.2.9 Interpolated beam profile for a 1000 eV beam captured two ports downstream from the source, with SNR values 58.9 (left) and 60.1 (right).

The same procedure was repeated with a fresh source, at port 33 (2 ports from ion source). These results, shown below in Figure 3.2.9, are seen to be significantly more reliable. Both cases are well-formed beam spots that are readily observable above the background LAPD levels. The flux

rope on fit is remarkably close to the flux rope off fit, falling roughly 5% above the nominal value. In comparison to the low SNR values of the port 31 case, the signal-to-noise values attributed to these spots suggests 10% or less noise-attributed error.

3.2.6 Experimental Conclusions

Combining the results from the past sections on experimental data, we have clearly observed radial ion beam broadening in the presence of flux ropes. The broadening is well-above the detection limit of our present hardware – our particle collection scheme is sensitive to changes on the order of 1 mm, while beam broadening on the order of 0.4 cm was observed. The enhanced broadening appears to be maximized for lower-energy ion beams. Enhanced broadening is also observed for ions with longer transit times (collected further downstream). The biggest issue presented when working through ion beam data is the presence of enhanced electrical noise attributed to the powerful flux rope discharge events occurring every cycle. As shown in Sections 3.1.1 and 3.1.4, convolution of noise with the ion beam signals represents a particularly thorny pitfall one must be mindful of. This made acquisition of lower-energy signals quite difficult. At extended distances from the ion source, the 500 eV beam could not be recaptured due to a combination of electrical noise and attenuated beam signal attributed to a dying ion source.

Chapter 4
Modeling and Simulation

4.1 Coulomb Collisions and Turbulent Modeling

In order to better understand the experimental results, we looked at possible interactions between fast ions and three potential broadening mechanisms: Coulomb scattering, magnetic fluctuations, and electrostatic fluctuations. Using estimates for the wave amplitudes and particle parameters obtained via experiment, estimates for the observed fast ion spreading were calculated. These values are then compared to spreading observed in experiment to determine the validity of the models used.

4.1.1 Transport Predicted from Coulomb Collisions

Past work by the Irvine Fast Ion Group has extensively covered fast ion broadening due to Coulomb scattering. In general, an ion beam passing through a background plasma is observed to broaden due to Coulomb interaction with the singly-ionized background Helium plasma. Early work by Liangji Zhao helped to confirm that the test ion beam is diffusive when these scattering events takes place, [12] leading to broadening of the form:

$$FWHM^2 = 8\ln 2[\langle(\Delta r_0)^2\rangle + \langle(\Delta r)^2\rangle] \quad (4.1)$$

$$= 5.545[\langle(\Delta r_0)^2\rangle + 2D_{perp}t] \quad (4.2)$$

where:

$$D_{perp} = \langle(\Delta r)^2\rangle / 2t \quad (4.3)$$

is the perpendicular diffusion coefficient for a set of plasma parameters and $\langle(\Delta r_0)^2\rangle$ is the radial displacement of a fast ion. $\langle(\Delta r_0)^2\rangle$ is found by fitting the simulated data ensemble at 0 ports (the

point of launch) to determine initial beam width. In the absence of electromagnetic turbulence, Coulomb scattering of this form is expected to be the primary diffusive mechanism interacting with the ion beam. Once obtained, the perpendicular diffusion coefficient can be compared to an equivalent analytic form of equation 4.3:

$$D_{perp} = v^2 \cos\theta^2 \nu_{PAS} / 4\Omega \qquad (4.4)$$

4.1.2 Transport Predicted from B-fluctuations

Process	Timescale (s)
Gyro-orbit time	3.5e-6
Pitch angle scattering time	5.0e-3
Flux rope flop time	1.4e-5
Coulomb energy loss time	6.0e-4

Table 4.1.1 Table of relevant time scales associated with ion-flux rope interaction.

Magnetic fluctuations from the flux ropes may be one potential candidate to explain increased fast ion transport beyond Coulomb scattering levels. As shown above in table 4.1.1, the fast ion gyro-orbit time is more than an order of magnitude faster than timescale for the flux ropes. Ergo, we will employ the assumption that fast-moving particles transiting through a flux rope region will see a time-stationary snapshot of the flux ropes' fields. An orbiting fast ion particle that interacts with the magnetic fluctuations is expected to receive an impulse from the interaction that will gently modify the orbit. We can use our assumption that particle energy will largely be conserved (as is generally the case with magnetic interactions with charged particles). Conservation of energy dictates that the change in perpendicular momentum (Δp_{perp}) will be equal to the change in axial momentum (Δp_z) scaled by the ratio of the momenta (p_{perp}, p_z):

$$p_z \Delta p_z + p_{perp} \Delta p_{perp} = 0 \rightarrow \Delta p_{perp} = p_z \Delta p_z / p_{perp} \qquad (4.5)$$

Which can be further simplified by replacing the momentum ratio with the velocity ratio of the given components. In the model being considered, a gyro-orbiting particle will briefly transit through a turbulent region each period, as shown in figure 4.1.2 below.

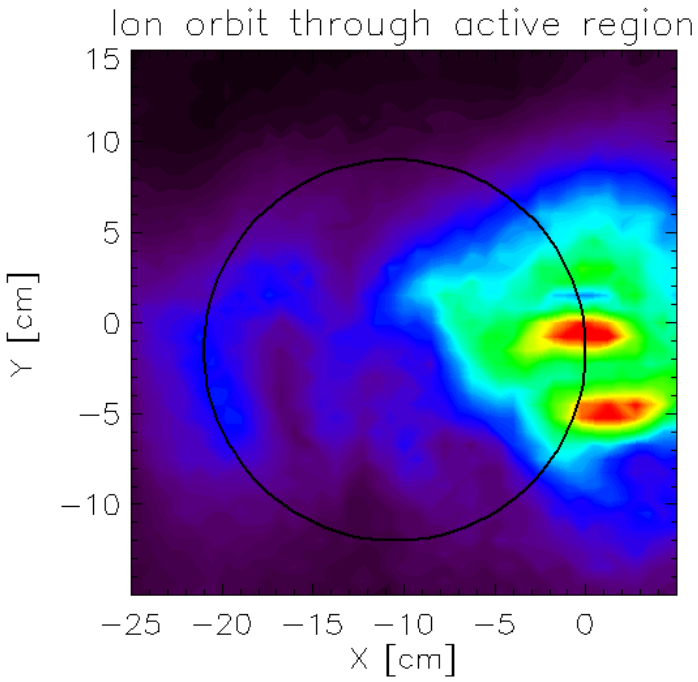

Figure 4.1.2 Figure illustrating a 1000 eV fast ion orbit (solid black line) through flux rope region. Contour plane represents perpendicular magnetic field strength, with a maximum of ~7 G.

In doing so, the particle experiences a "kick" from the interaction region. The kick experienced in one cycle, Δp_z, can be rewritten as an integral of the force experienced by the particle over an interval of time. For an ion deflected by the magnetic field via Lorentz force, this is approximated as:

$$\Delta p_z = \int F_z \, dt \leq q \, v_{perp} \, \delta B_{perp} \, \Delta t \qquad (4.6)$$

where q is the fundamental electron charge, v_{perp} is the perpendicular velocity of the gyro-orbiting particle, δB_{perp} is the maximum magnetic field strength, and Δt is the total time spent in the active region. Using this relation to simplify equation 4.5 yields:

$$\Delta p_{perp} = v_z \Delta p_z / v_{perp} = q v_z |\delta B_{perp}| \Delta t \qquad (4.7)$$

In our case, however, only a portion of the orbit has appreciably fluctuating fields. As such, we introduce a new factor *"f"* as the fraction of the orbit spent in the active region. For a single orbit, the time spent in the active region will be:

$$\Delta t = \tau_{gyro} \cdot f \qquad (4.8)$$

Allowing equation 4.7 to be rewritten as:

$$\Delta p_{perp} = q\ v_{perp}\ |\delta B_{perp}|\ 2*f*\pi\ /\ \Omega \qquad (4.9)$$

This result must be understood in the context of ensemble-averaged data in order to be compared to experiment. The relevant experimental data consists of an ensemble of particles taken over many shots. The resulting ion beam profile is quantified by a time-averaged FWHM, which represents the total radial beam size. When the effect in equation 4.9 is experienced by a collection of fast ions being kicked in different directions, the observed result will be radial spreading of the form:

$$\Delta r = \Delta \rho = \Delta v_{perp} / \Omega \rightarrow 2\pi f v_z |\delta B_{perp}| / \Omega B_0 \qquad (4.10)$$

$$\langle (\Delta r)^2 \rangle = (1/2) \cdot (2\pi f v_z |\delta B_{perp}| / \Omega B_0)^2 \qquad (4.11)$$

Taking the resulting equation and inserting nominal values for an 1000 eV ion beam (1000 eV, v_z/Ω=13.9 cm, B_0= 700 G, $|\delta B_{perp}|$~7 G, f~0.2) we can obtain a value for predicted spreading per orbit. Equation 4.11 predicts spreading on the order of 0.001 cm^2/orbit. While this is an

appreciable effect over many orbits, present hardware does not have the ability to resolve changes of this magnitude.

4.1.3 Transport Predicted from E-fluctuations

Another potential mechanism for enhanced fast ion transport is electrostatic fields related to the flux rope electron beam. As was the case in the previous section, fast ions traveling through the flux rope region interact with a time-stationary snapshot of the electrostatic fields generated by the flux ropes. Guiding center drifts are observed to be experienced by magnetized, gyro-orbiting particles in the presence of an external field. This takes on the general form:

$$v_{drift} = (F \times B)/q|B|^2 \qquad (4.12)$$

In this case, the external field is the Lorentz force due to the electric field. Substituting in the Lorentz force, and solving for the displacement in the drift direction yields:

$$\Delta r_e \sim (\delta E/B_0)\tau_{gyro} \qquad (4.13)$$

for a particle immersed in a fluctuating electric field. As previously described in Section 4.1.2 above for magnetic fluctuations, it is necessary to introduce the *f* coefficient to account for the time spent in the active region. Equation 4.13 then becomes:

$$\Delta r_e \sim (\delta E/B_0)\tau_{gyro}\cdot f \qquad (4.14)$$

$$\langle(\Delta r_e)^2\rangle = (1/2)\cdot((2\cdot\delta E/B_0)\tau_{gyro}\cdot f)^2 \qquad (4.15)$$

Evaluating equation 4.15 with nominal values for background magnetic field, average gyro-orbit time, and *f* allows an estimate to be obtained for any size electrostatic field. For a particle with a given gyroperiod traveling through an electrostatic field with similar properties to LAPD flux ropes ($\delta E \sim 200$ V/m, $B_0 = 0.07$ T, $\tau_{gyro} \sim 6.5$ μs, $f \sim 0.21$), spreading on the order of 0.3 cm^2 is

predicted for 1000 eV and 700 eV ion beams collected 2 ports downstream. The transit time of the 500 eV is different from the other parameters sets at this location. Evaluating for the same parameters, but substituting τ_{gyro}~13 μs yields 1.22 cm^2. Unlike the previous section, a change of this magnitude should be readily observable with our present hardware. However, the behavior of equation 4.15 suggests that significant spreading can be observed for beams that make many orbits.

4.2 Background Modeling and Simulation

4.2.1 Monte Carlo Test Beam Simulation via IDL

Experimental results can be compared to simulated test ions. Simulation is carried out through a Monte Carlo-based particle-tracing code developed within IDL by the UC Irvine Fast Ion Group. Functionally, the routine simulates a test beam of singly-ionized Lithium ions through a background singly-ionized plasma with user-supplied plasma properties mimicking those of the LAPD. Individual particles are initialized with some random deviation from the known energy and launch position as governed by the energy/spatial divergence of our ion gun. Upon initialization, a particle will perform an integer number of gyro-orbit prior to being collected into a data array for further analysis upon run-time completion. A schematic overview of the simulation routine is shown below in Figure 4.2.1.

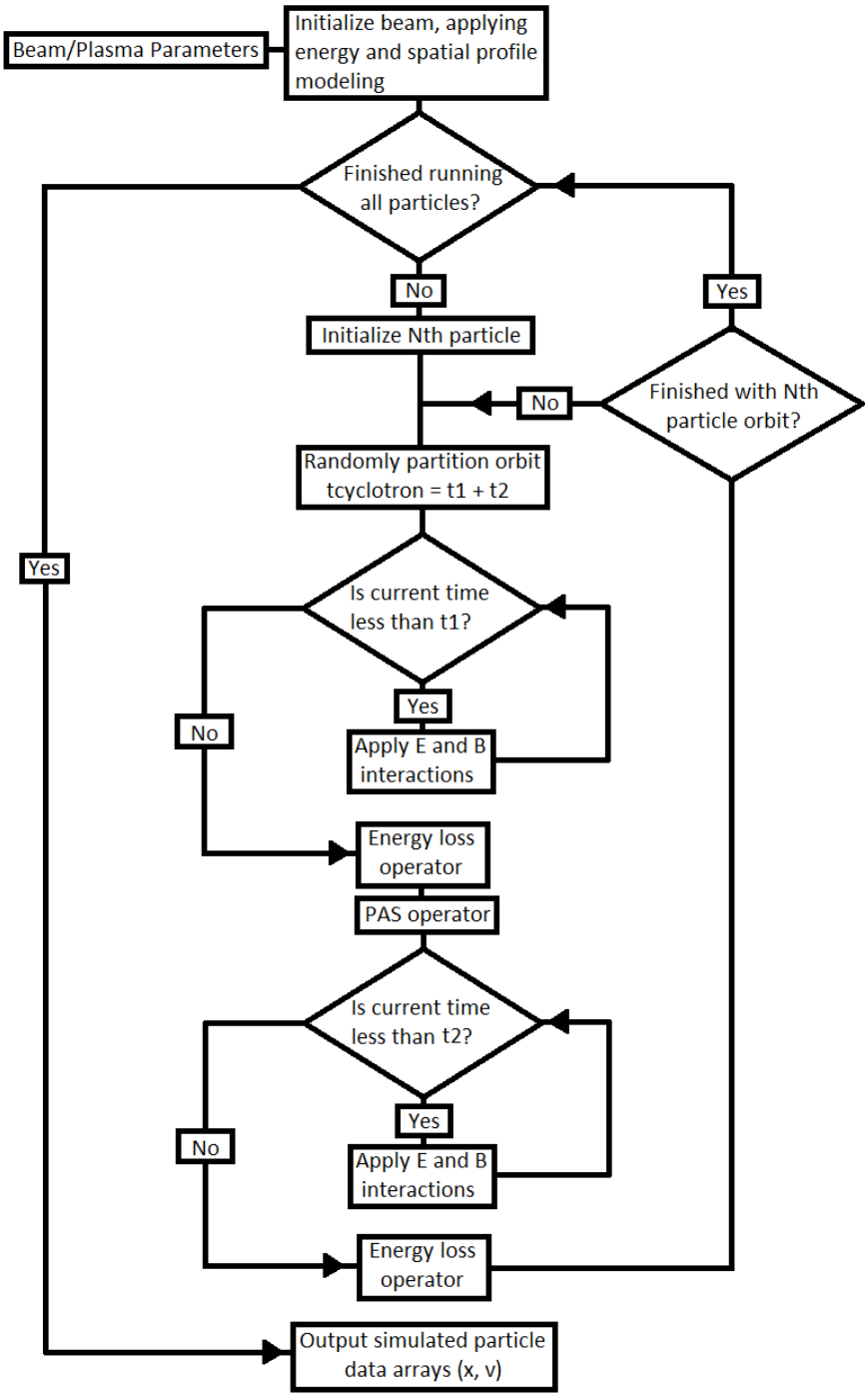

Figure 4.2.1 Block diagram of Monte Carlo simulation. Upon output of the data arrays, the data is run through a synthetic detector routine that emulates the behavior of the collector probe. Once this is completed, the simulated data is analyzed by the same fit functions as experimental data.

Implicit in this treatment of fast ion interactions is the assumption that the Coulomb, magnetic, and electrostatic effects can be treated as linearly additive diffusive effects on an unperturbed

beam. Past work by Shu Zhou has demonstrated the validity of this approach for fast ions experiencing Coulomb collisions with background plasma in the presence of electrostatic fluctuations. [15] This assumption is further justified by looking at the relative magnitude of the Lorentz force perturbation from δE and $[(v + \delta v) \times \delta b]$ relative to the background motion, $(v \times B_0)$. Evaluating the force ratios, $F_{\delta E}/F_{(vxB0)}$ and $F_{\delta B}/F_{(vxB0)}$, yields ratios of 9% and 1% respectively. The perturbing forces are localized near the magnetic axis, further diminishing their effect relative to the persistent background gyromotion – orbit-averaging drops the ratios to 2- to 3-orders-of-magnitude below the background motion.

A new modeling concern arises in this experiment as a result of interacting our fast ion beam with magnetic flux ropes, primarily located on the magnetic axis. In order to create a "good" region of interaction, the ion gun must be pulled back from the magnetic axis by approximately two fast ion gyroradii, thereby allowing the fast ion beam to pass through the turbulent region for a portion of the orbit. In doing so, we break the axisymmetric orbit of the fast ion beam, and the simple density result from the microwave interferometers can no longer be taken as true.

To fix this, an IDL modeling routine is created to determine the effective electron density experienced by a particle on such an asymmetric orbit. The routine acts to overlay a generic fast ion orbit onto a model of the two dimensional electron density profile. The program then samples the density 1000 times along the orbit at equal intervals (roughly every millimeter) before computing the orbit averaged value. This is shown to be a reasonable model due to the fact that the slowing down time is much larger than the cyclotron period ($\Omega_c * \tau_{slow} \sim 160 >> 1$).

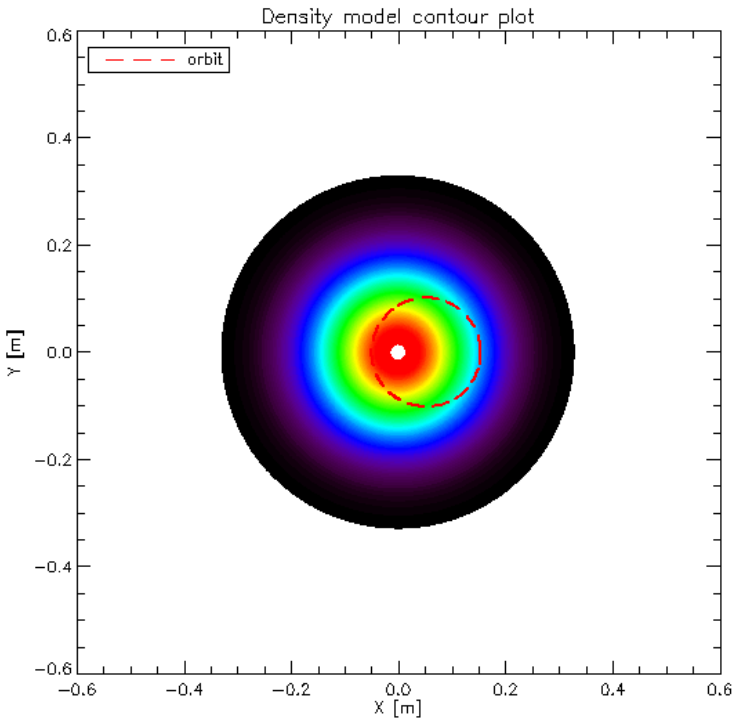

Figure 4.2.2 Orbit-averaged density model cartoon. The colored contour represents a density gradient constructed from a combination of LAPD data and modeling. The dashed red line corresponds to the orbit over which the density will be sampled and averaged.

Number of Turns	1000 eV beam's effective n_e [cm^{-3}]	700 eV beam's effective n_e [cm^{-3}]	500 eV beam's effective n_e [cm^{-3}]
1	9.82e11	1.46e12	
2	9.82e11	1.46e12	1.34e12
3	1.14e12		1.48e12
4	1.10e12		
5		1.33e12	

Table 4.2.3 Table of orbit-averaged density values

The modified density, in addition to background properties and discharge parameters, is supplied to the simulation. Upon judicious choice of total particles to iterate, the routine can be run to completion and analyzed by accompanying FWHM fitting routine (described earlier in Section 2.5.3). Results presented below are for ensembles of 250,000 test particles. To ensure a valid comparison can be made, simulation values that call a random number generator (e.g. fast ion phase) are generated from the same starting seed every time, removing the random nature of this

operator's output.

With necessary plasma and ion beam parameters supplied to the Monte Carlo simulation, results for nominal spreading of the ion beam due to Coulomb spreading are readily obtained. A test ion beam is observed to experience radial FWHM spreading as the result of Coulomb interactions with the background plasma. Increased radial FWHM's are observed for increasing number of rotations about the magnetic axis (shown for the 1000 eV test beam in Figure 4.2.5).

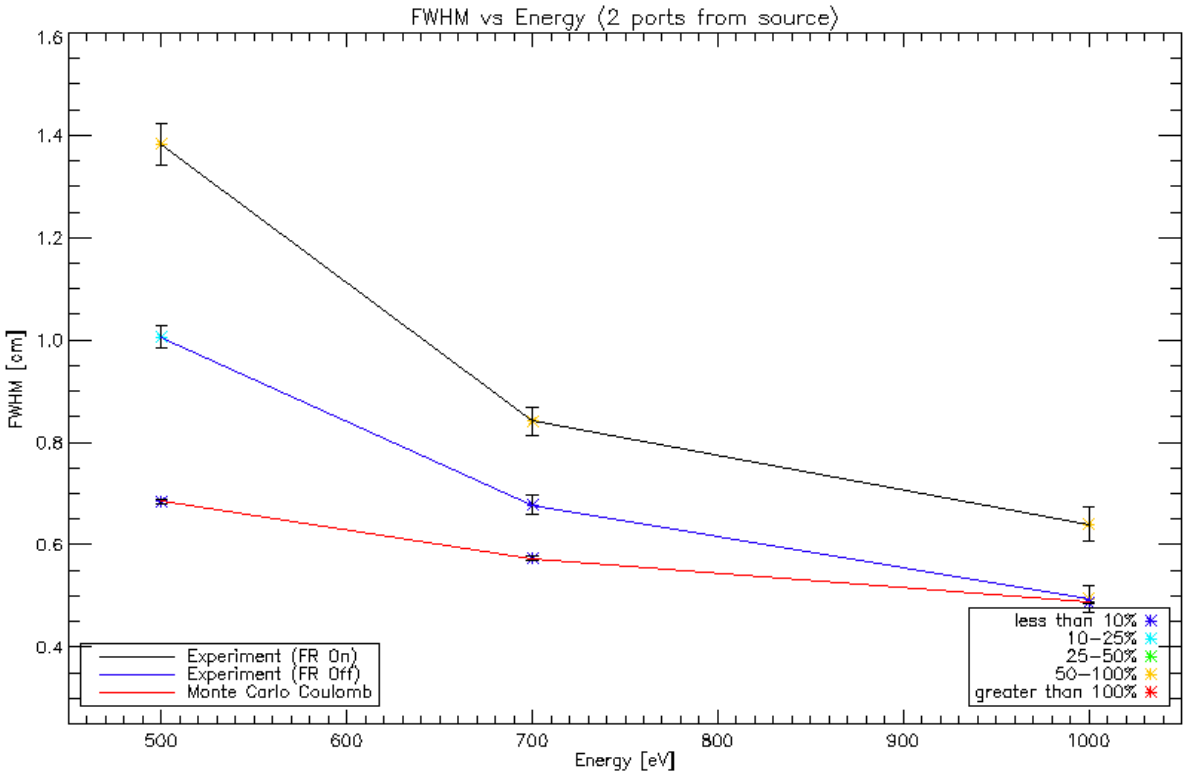

Figure 4.2.4 Simulated beam spot vs. energy for fast ions experiencing Coulomb scattering. Experimental results from the previous section are included for comparison. Error bars and SNR fit values are included for all data points.

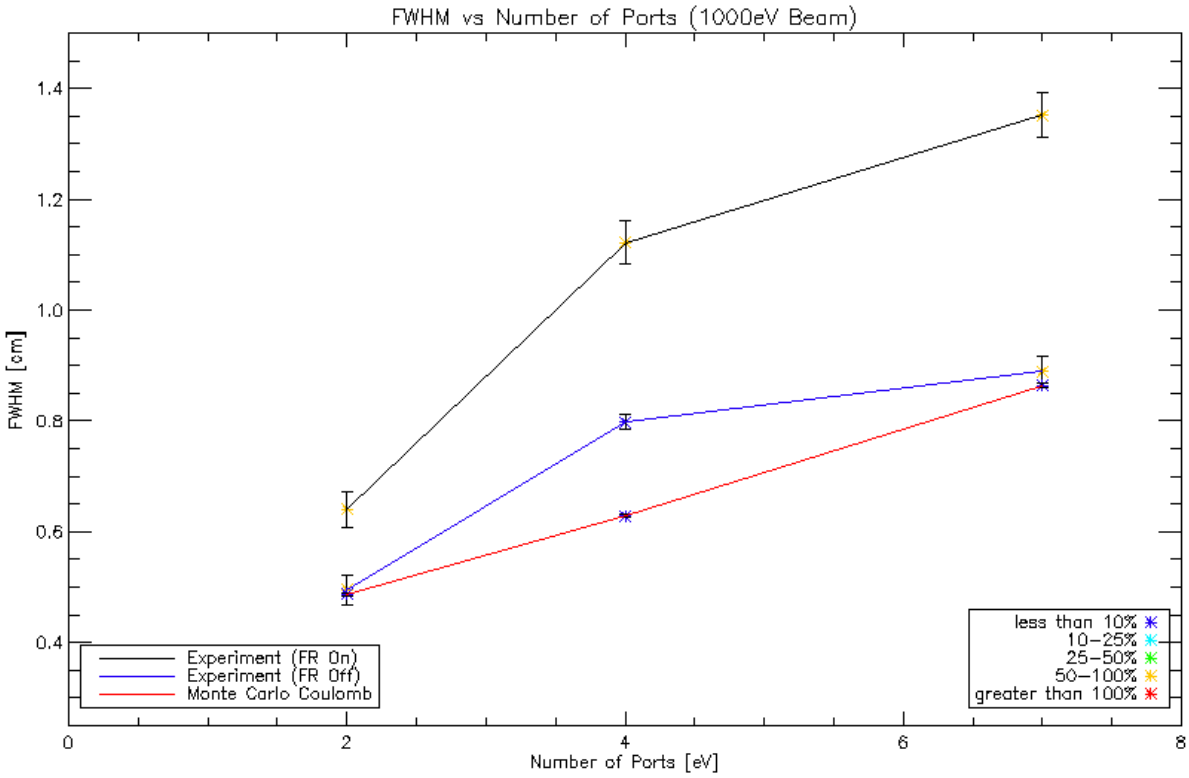

Figure 4.2.5 Simulated beam spot vs. distance for a 1000 eV ion test beam experiencing Coulomb scattering. Experimental results from the previous section are included for comparison. Error bars and SNR fit values are included for all data points.

As shown above, the ion beam is observed to broaden in the presence of Coulomb collisions. This broadening is minimized at high energy. This is a result of the higher-inertia beam being less perturbed by the Coulomb-Coulomb collisions compared to a similar ion beam of lower energy. This result has been independently verified through past research performed by Liangji Zhao [12], Shu Zhou [15], et al.

In the case of the FWHM vs port scan presented in figure 4.2.5, it is possible to quantify the Coulomb spreading via the beam fits (equation 4.3). The 1000 eV fit FWHM is observed to increase linearly with port number, resulting in a fit diffusion coefficient of ~830.1 cm^2/s, consistent with the calculated value of ~940.2 cm^2/s obtained via equation 4.4. This result is expected – Diffusive spreading attributable to Coulomb broadening has already been observed and quantified by Shu Zhou. These results are consistent with published observations on

interactions with background plasma. [15] Monte Carlo simulations are observed to contain negligible error in the FWHM fit for the Coulomb-only case.

4.2.2 Simulating Magnetic Turbulence

In order to simulate interactions with magnetic turbulence, the Monte Carlo simulation is supplied with a time-stationary magnetic field array. During runtime initialization, the magnetic field data file is read in, converted to the appropriate unit set, and passed along to the particle's orbit integrator. The two-dimensional array contains equidistant field data along a two-dimensional grid. The orbit integrator then interpolates intermediate spatial locations as necessary.

It should be noted that the reconstructed magnetic field plane data, whose analysis was described earlier in section 3.1.2, is not constructed from simultaneously measuring all points on the 2D grid. Instead, a single, moving probe takes data at a single location over repeated shots before being moved to the next location where the process begins again until all grid points are sampled. As such, the plane data represents average values of δB_{perp}.

Test ions will see the strongest magnetic field signal near the magnetic axis, as shown below in figure 4.2.6. The magnetic field profile used in simulation has not been divergence cleaned (div·B has not been forced to zero). This will likely increase the spreading observed from the magnetic field resulting from the addition of non-physical noise in the profile. Given that the overall magnitude of the effect is expected to be small, the modification to the beam fit is also expected to be small, and thus has not been treated.

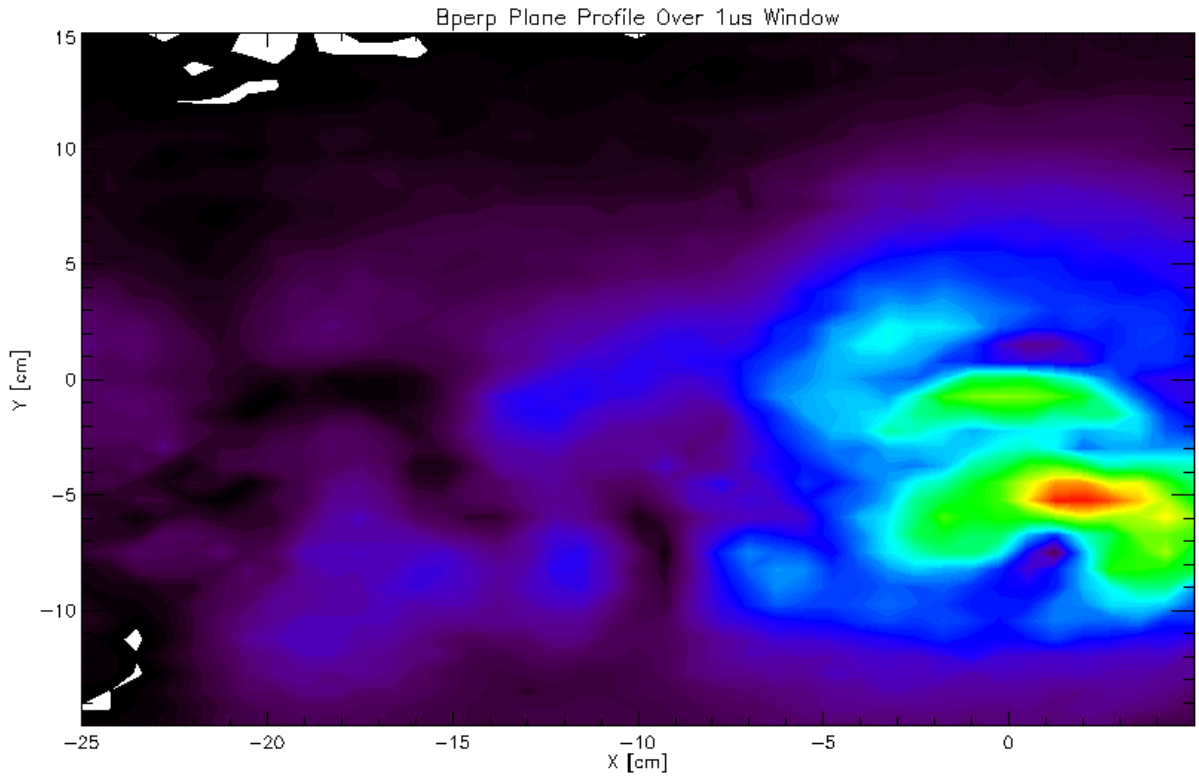

Figure 4.2.6 Magnetic field profile for perpendicular field component near the magnetic axis. Peak field strength is ~7 G.

Upon runtime completion of the Monte Carlo simulation, the test ion data is then processed through a synthetic detector program as per the earlier Coulomb spreading results. The resulting beam contour, an example of which is shown below for 700 eV (Figure 4.2.7), shows minimal spreading above background levels fit in the previous section. Carrying through this simulation procedure for the range of energies and collection locations we are interested in yields profiles in the energy- and time-domains. Results for subsequent ion beam simulations show minimal deviation from the background (Figure 4.2.8).

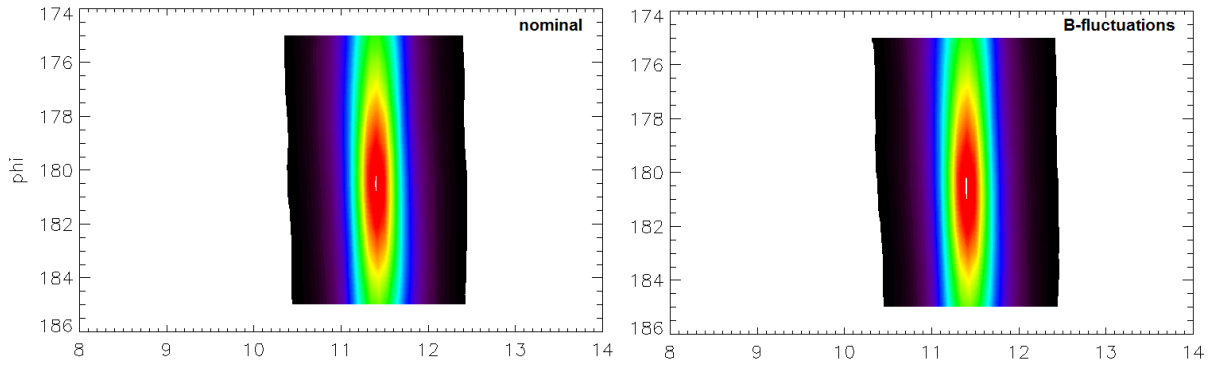

Figure 4.2.7. Comparison between Monte Carlo simulation results for a nominal beam and a beam passed through magnetic fluctuations shown above. The fit FWHM are nearly identical in this case, with fits of 0.573 cm (nominal) and 0.580 cm (B-fluctuations).

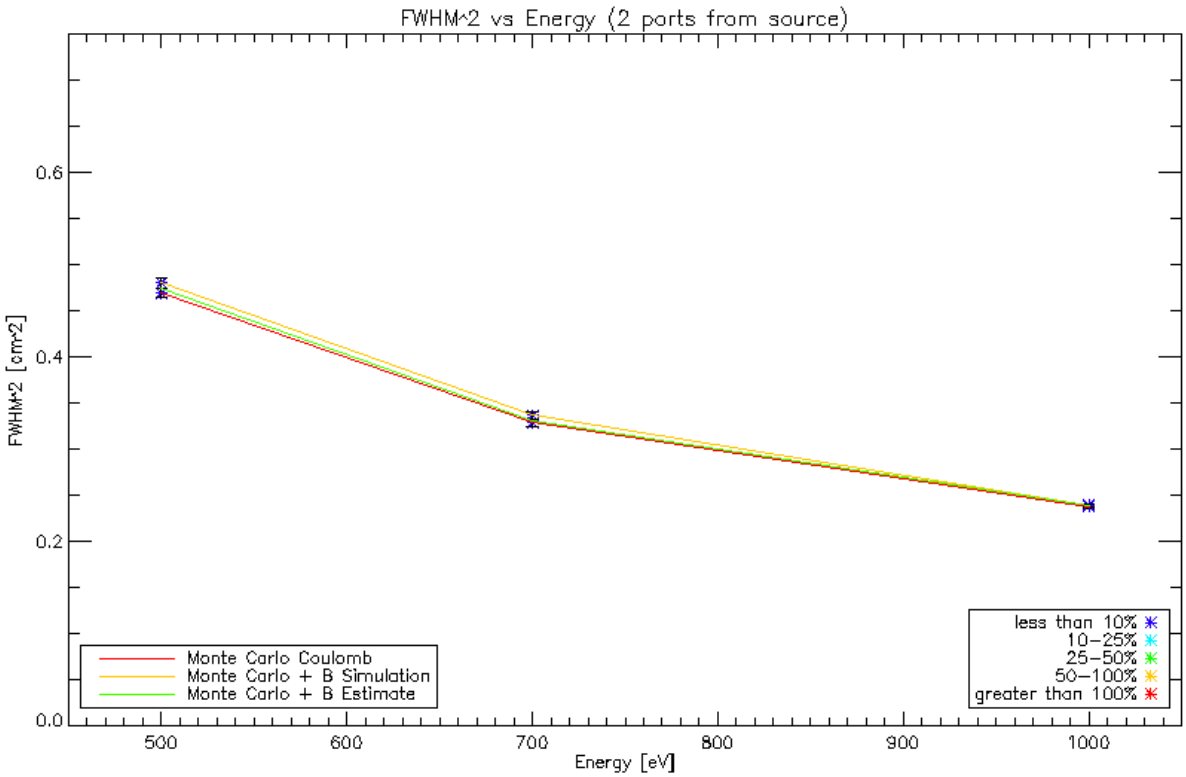

Figure 4.2.8 Comparison between Coulomb-scattered Monte Carlo simulation results to Monte Carlo simulation with magnetic fluctuations included. Expected values based on the predictions in section 4.1.3 are included in green. While a minor increase is observed at all energies, the magnitude of the change is not experimentally observable.

4.2.3 Simulating Electrostatic Turbulence

Electrostatic field data is used in Monte Carlo simulation in the same manner as the magnetic field data discussed in the previous section. Electrostatic fluctuating field data is supplied to the

Monte Carlo simulation upon runtime initialization, wherein the data array is converted to the appropriate physical units before being passed along to the orbit integrator. Test fast ions are then allowed to perform helical gyromotion until “recaptured” by the Monte Carlo simulation at the specified x-y collection plane.

After initialization, the electric field data file is passed along to the particle's orbit integrator and used in the same procedure as the magnetic field data.

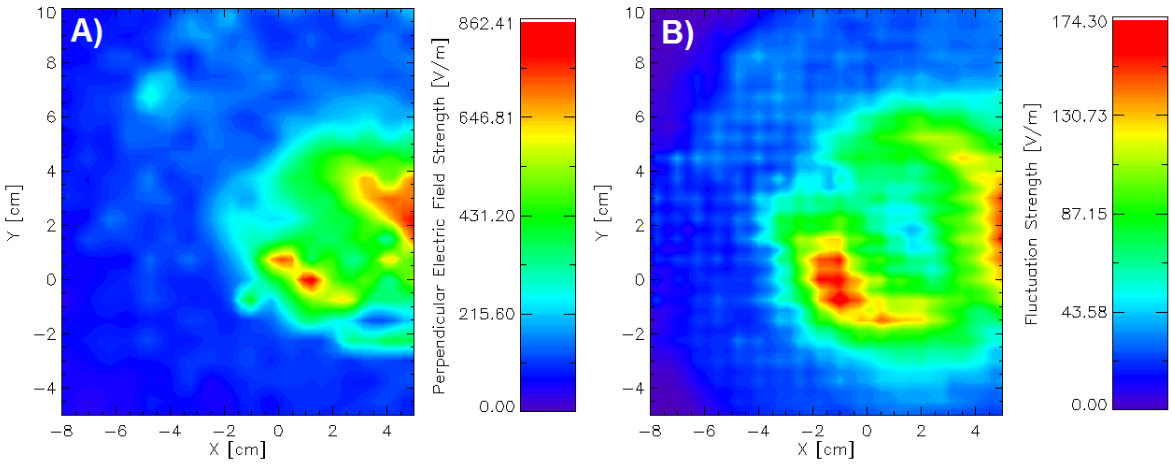

Figure 4.2.9 Electric field profile for perpendicular field component near the magnetic axis. Peak field strength is ~860 V/m.

In contrast to the previous section on magnetic turbulence (where no appreciable modification to spreading was observed), fast ion profiles in the presence of such an electrostatic field are observed to considerably broaden. For a 700 eV beam performing one gyro-orbit, the beam is observed to spread an additional 2.7 millimeters above the nominal Coulomb spreading value, as shown below in Figure 4.2.10.

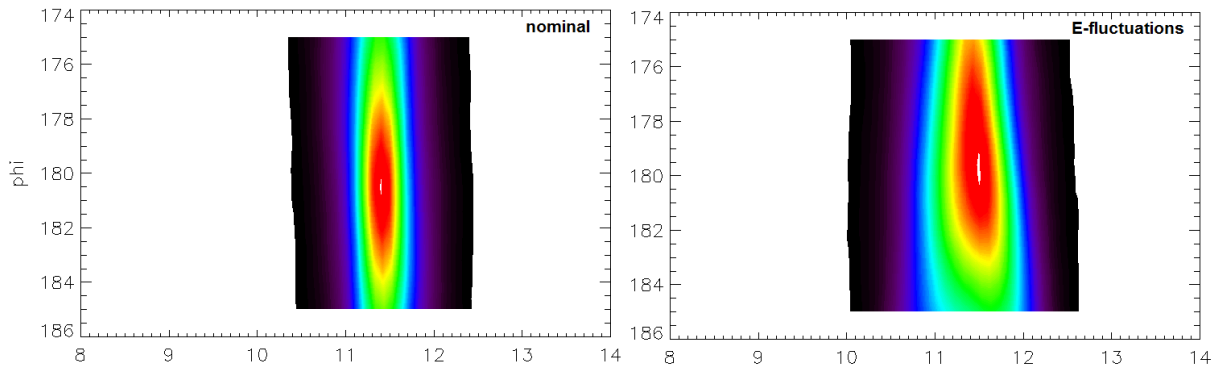

Figure 4.2.10 Comparison between Monte Carlo simulation results for a nominal beam and a beam passed through electrostatic fluctuations shown above. The fit FWHM are quite disparate in this case, with fits of 0.573 cm (nominal) and 0.846 cm (E-fluctuations).

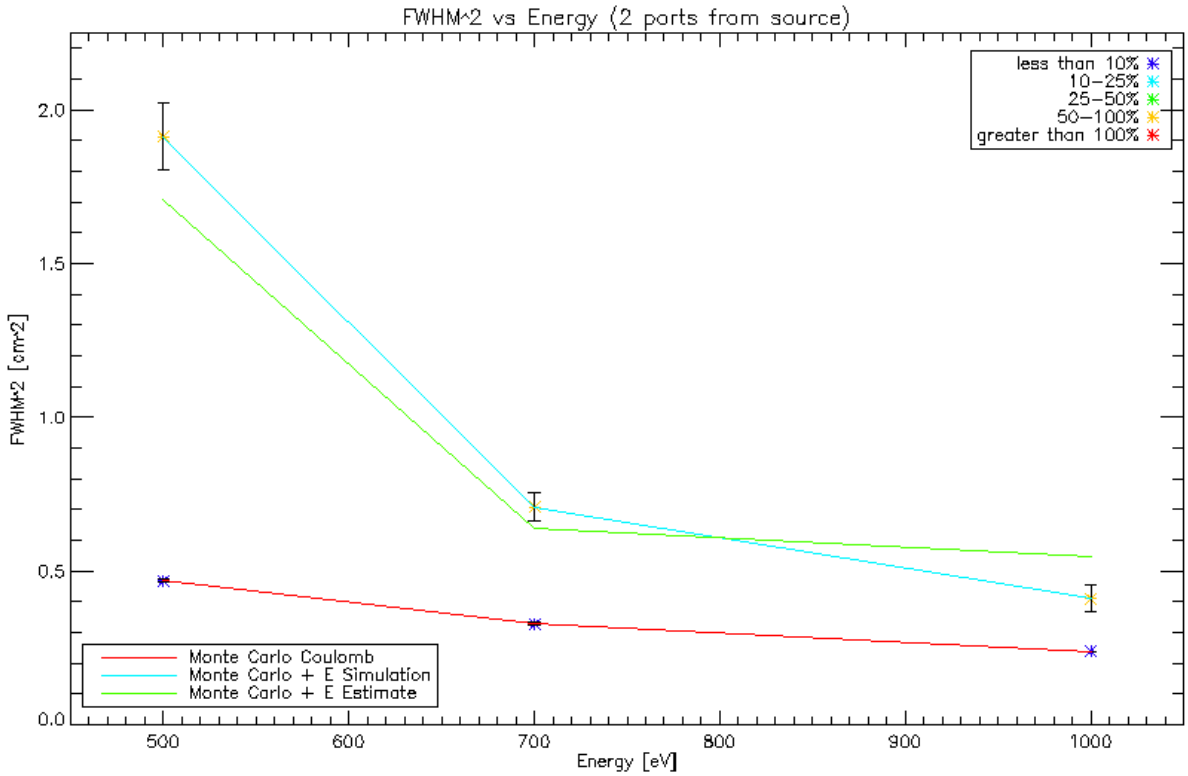

Figure 4.2.11 Comparison between nominal Monte Carlo simulation results to Monte Carlo simulation with electrostatic fluctuations included. Expected values based on the predictions in section 4.1.3 are included in green. Significant spreading is observed across all energies.

From Figures 4.2.10 and 4.2.11, it is obvious that the introduction of electrostatic turbulence into the Monte Carlo simulation produces additional spreading. The magnitude of the increased spreading is on the order of 3-14 millimeters, which is readily observable by our present

hardware.

The complete simulation results for both types of turbulence are collected and shown in the three figures below. The first figure shows how a 1000eV test beam is influenced for longer transit times (larger distance downstream). The latter figures shows the results obtained for beams collected 2 ports (dz~64 cm) and 4 ports (dz~128 cm) downstream for a range of ion beam energies. In both cases, the observed increase in spreading does not appear to be attributable to the magnetic field perturbations. Spreading observed in the presence of electrostatic turbulence results in beam spreading on the same order as experimental results discussed in section 3.2.

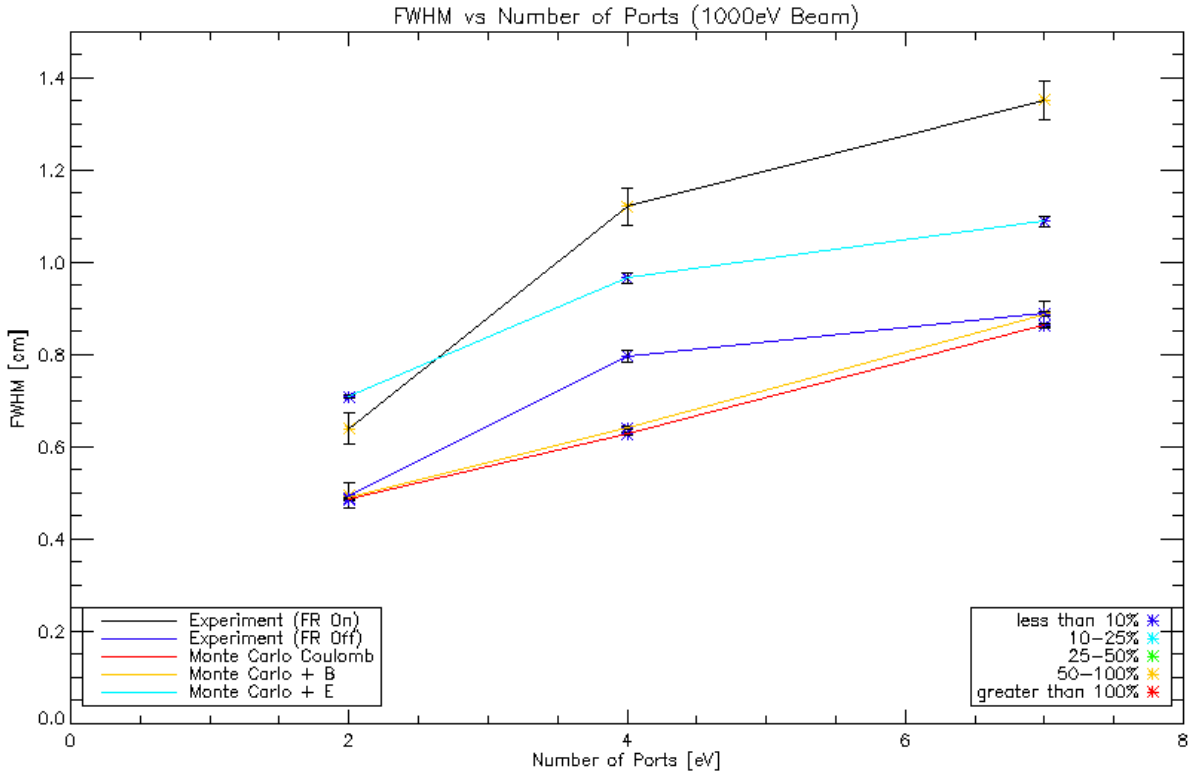

Figure 4.2.12 FWHM vs number of ports for 1000 eV test ions simulated via Monte Carlo simulation. Launch parameters for the beams can be found in table 3.1.2.

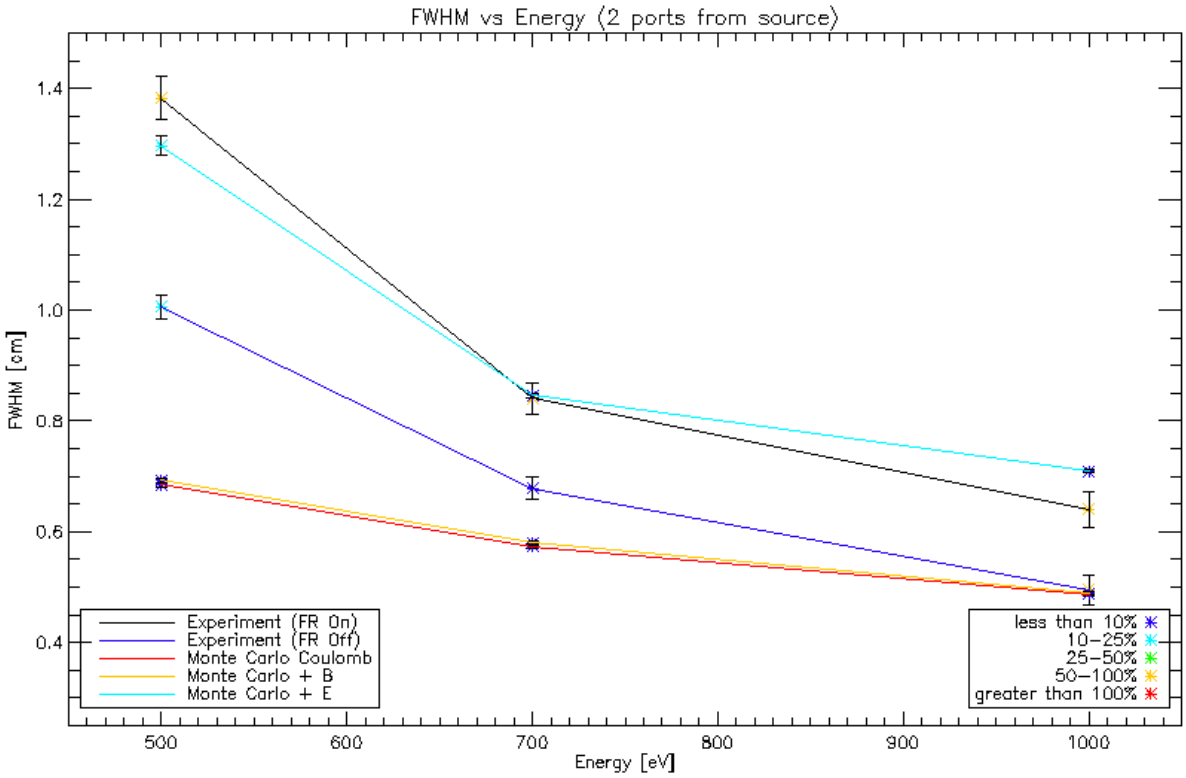

Figure 4.2.13 FWHM vs Energy for test ions simulated via Monte Carlo simulation. All ion beams are recaptured 2 ports downstream (~64 cm).

4.3 Simulation and Modeling Conclusions

Fast ion transport is nominally affected by Coulomb scattering, which has been well-documented in past work. Enhanced transport beyond the classical levels appears to be attributable to electrostatic fluctuations from the flux rope, localized primarily along the magnetic axis. Magnetic perturbations associated with this effect appear to have negligible impact on beam spreading. The time evolution of the fast ion beam width is observed to be classically diffusive in the Coulomb case, whereas the time evolution in the presence of flux ropes is enhanced significantly above these values.

Chapter 5
Conclusions

5.1 Summary

In this thesis work, the interaction between a fast ion beam and a set of warm, axially propagating electron streams constituting flux ropes are explored and profiled. The main approach to study the fast ion transport in the presence of various forms of turbulence described in this thesis work involves launching lithium fast ions as test particles into the background Helium plasma. During the flux rope discharge, the plasma parameters such as electron density, electron temperature, and the amplitude of the density gradient are all appreciably modified from the background values. The strength of the perturbation from the flux rope is modified by changing the discharge current and voltage. In this experiment, the fast ion beam is treated as a set of test particles and the turbulent waves are treated as background. The fast ion transport is observed to decrease with increasing fast ion energy, while increasing with particle transit time (distance from the source). These experimental observations are also consistent with test particle Monte Carlo simulation results.

5.2 Future Work

The original goal of the previous experiment was to observe fast ion transport by magnetic fluctuations. This goal was not achieved. To access a condition where transport is dominated by magnetic fluctuations, the ratio of $\delta B/\delta E$ needs to be two orders of magnitude larger. This regime is presently well-beyond the capabilities of our hardware. A more promising, alternative exploration can be performed with a much higher energy beam. The electrostatic transport has been shown to decreases with energy while magnetic transport does not, [17] suggesting the ability to minimize electrostatic transport at sufficiently high beam energy. Future work

profiling the secondary cathode-anode shifted case could help to explain enhanced spreading during the anode-shifted condition. Further work synchronizing the B-dot and fast ion collector data acquisition may help to more accurately model single shot field profiles during the discharge phase.

To form a complete picture, it is desirable to further include simulation results for fast ions gyro-orbiting through anode-shifted flux ropes. Unfortunately, plane data for this case is not presently available. Experimental results predict broadening above background levels that is presently unexplained, and which may be attributable to the electrostatic field in the shadow of the flux rope anode. Shifting the flux rope anode downstream closer to the secondary cathode could help illuminate the underlying mechanism inducing fast ion transport. The setup described in Chapter 3 can be modified by moving the flux rope anode from top rectangular port 13 to top rectangular port 41. In doing so, the plasma parameter modifications attributable to the flux rope discharge are further modified. Triple probe line scans indicate a reduced electron temperature behind the shifted anode, while magnetic perturbations are largely absorbed at the anode. Despite the reduced turbulence in the shadow of the anode, additional fast ion spreading beyond the Coulomb level is observed in experimental data, necessitating further work in this area.

Potential improvements to the diagnostic tools employed could also benefit future extensions of this experiment. Specifically, a high bandwidth particle collector could shed light on the time evolution of active region near the magnetic axis during the flux rope discharge. The fine structure and temporal evolution of these ropes is not well-understood, and further explorations of the active region may prove beneficial for upgraded simulation and modeling efforts. To this end, an upgraded diagnostic tool may aid in the rejection of bad data shots, which has proven problematic previously. The ability to passively discriminate (or otherwise remove) unusable

data would be immensely beneficial.

Appendix A – Source file locations

Description	HDF5 Filename
4 port 1000eV Beam Anode-Shifted	ANODE_SHIFT_plus5x_1000ev_13p9cm_53p9deg_0p5tpp_P31 2014-01-25 12.08.18
2 port 1000eV Beam Anode-Shifted	ANODE_SHIFT_plus5x_1000ev_13p9cm_53p9deg_0p5tpp_P33 2014-01-25 15.02.45
B-dot line scan 160V FR	B_line_P33mov_P26ref_160V_good_resolution 2014-01-24 18.41.47
B-dot plane scan 160V FR coarse plane	bfield1-overnight-700G-p27mov-p26fixed 2014-01-20 21.26.49
B-dot plane scan 160V FR fine plane	bfield2-overnight-700G-p27mov-p26fixed-fine-resol 2014-01-21 20.08.57
B-dot ISAT line scan 110V FR	B-Isat_xline_110V 2014-01-23 09.46.20
B-dot ISAT line scan 160V FR	B-Isat_xline_160V 2014-01-22 11.28.01
Anode-shifted line scans	B-Isat_xline_160V_anodep41 2014-01-25 09.28.12
B-dot ISAT line scan 260V FR	B-Isat_xline_260V 2014-01-22 10.49.09
4 port 1000eV Beam	FI_1000ev_700G_0pt5tpp_53pt9deg_13pt9cm_P31_find_beam_active 2014-01-21 10.47.28
2 port 1000eV Beam	FI_1000ev_700G_0pt5tpp_53pt9deg_13pt9cm_P33 2014-01-20 20.01.19
4 port 1000eV Beam	fine_grid_FI_1000ev_700G_0pt5tpp_53pt9deg_13pt9cm_P31_find_beam_active 2014-01-21 11.31.24
4 port 1000eV Beam -2.5cm w.r.t. magnetic axis	fine_grid_shift_minus_2pt5_TAKE_TWO_FI_1000ev_700G_0pt5tpp_53pt9deg_13pt9cm_P31 2014-01-21 16.31.18 (2)
4 port 1000eV Beam -5.0cm w.r.t. magnetic axis	fine_grid_shift_minus_5_FI_1000ev_700G_0pt5tpp_53pt9deg_13pt9cm_P31 2014-01-21 17.32.52
4 port 1000eV Beam -7.5cm w.r.t. magnetic axis	fine_grid_shift_minus_7pt5_FI_1000ev_700G_0pt5tpp_53pt9deg_13pt9cm_P31 2014-01-21 18.29.47
4 port 1000eV Beam +2.5cm w.r.t. magnetic axis	fine_grid_shift_plus_2pt5_FI_1000ev_700G_0pt5tpp_53pt9deg_13pt9cm_P31_find_beam_active 2014-01-21 12.40.41
4 port 1000eV Beam +5.0cm w.r.t. magnetic axis	fine_grid_shift_plus_5_FI_1000ev_700G_0pt5tpp_53pt9deg_13pt9cm_P31_find_beam_active 2014-01-21 13.34.07
4 port 1000eV Beam +5.0cm, 260V FR	fine_grid_shift_plus_5_FI_1000ev_700G_0pt5tpp_53pt9deg_13pt9cm_P31_FR_260V 2014-01-22 14.30.29
2 port 500eV Beam +5.0cm w.r.t. magnetic axis	plus5shift_FI_500ev_1tpp_65pt4deg_P33 2014-01-23 13.14.54
2 port 700eV Beam +5.0cm w.r.t. magnetic axis	plus5shift_FI_700ev_0pt5tpp_45pt3deg_P33 2014-01-23 12.22.53

7 port 700eV Beam +5.0cm w.r.t. magnetic axis	plus5shift_FI_700ev_3over7tpp_52deg_11p38cm_P28_12A 2014-01-24 17.26.57
9 port 700eV Beam +5.0cm w.r.t. magnetic axis	plus5shift_FI_700ev_5over9tpp_50pt7deg_P29_12A 2014-01-24 12.43.36
2 port 1000eV Beam +5.0cm w.r.t. magnetic axis	plus5shift_FI_1000ev_0pt5tpp_53pt9deg_P33 2014-01-23 12.02.22
7 port 1000eV Beam +5.0cm, 11.5A heater	plus5shift_FI_1000ev_3over7tpp_46p6deg_12p55cm_P28_11p5A 2014-01-24 15.30.16
7 port 1000eV Beam +5.0cm, 12.0A heater	plus5shift_FI_1000ev_3over7tpp_46p6deg_12p55cm_P28_12A 2014-01-24 16.31.21
9 port 1000eV Beam +5.0cm, 12.0A heater	plus5shift_FI_1000ev_4over9tpp_48pt5deg_P29_RERUN_3_12A 2014-01-24 11.43.20
4 port 500eV Beam +5.0cm w.r.t. magnetic axis	shift_minus_5_FI_500ev_700G_0pt75tpp_56pt3deg_P31 2014-01-22 16.50.51
4 port 700eV Beam +5.0cm w.r.t. magnetic axis	shift_minus_5_FI_700ev_700G_0pt5tpp_45pt3deg_P31 2014-01-22 14.58.36
4 port 700eV Beam +5.0cm w.r.t. magnetic axis	shift_minus_5_FI_700ev_700G_0pt5tpp_45pt3deg_P31_RERUN 2014-01-22 15.56.52
4 port 1000eV Beam +5.0cm, 110V FR	shift_minus_5_FI_1000ev_700G_0pt5tpp_53pt9deg_P31_FR_110 2014-01-22 18.49.45
4 port 1000eV Beam +5.0cm, 260V FR	shift_minus_5_FI_1000ev_700G_0pt5tpp_53pt9deg_P31_FR_260_rerun 2014-01-22 18.58.41
SNR data for 10.0A heater	SNR_10A_P31 2014-01-22 12.21.48
SNR data for 10.5A heater	SNR_10500mA_P31 2014-01-22 13.10.29
SNR data for 11.5A heater	SNR_11500mA_P31 2014-01-22 12.46.50
700G 110V FR swept line	sweptprobe_700G_LaB6bias110V_p34xline 2014-01-24 09.16.24
700G 160V FR swept line anode-shifted	sweptprobe_700G_LaB6bias160V_anodep41_p34xline 2014-01-25 11.03.20
700G 160V FR swept plane	sweptprobe_700G_LaB6bias160V_p34mov 2014-01-23 20.14.32
700G 160V FR swept line	sweptprobe_700G_LaB6bias160V_p34xline 2014-01-24 09.47.30
700G 260V FR swept line	sweptprobe_700G_LaB6bias260V_p34xline 2014-01-24 08.41.09
700G 260V FR swept line	sweptprobe_700G_LaB6bias260V_p34xline 2014-01-24 08.46.00
700G 160V FR triple plane	triple_probe_700G_LaB6bias160V_p28fixed_p34mov 2014-01-22 21.55.21

Appendix B
250k Particle Monte Carlo Simulation Locations

Base folder: 'C:\Users\User\Data Analysis\250k Thesis MC Sims\'

Run Description	Run Location Subfolder
500eV, 2 port nominal	'\500ev\nom 2 port\'
500eV, 2 port magnetic	'\500ev\B 2 port\'
500eV, 2 port electrostatic	'\500ev\E 2 port\'
700eV, 2 port nominal	'\700ev\nom 2 port\'
700eV, 2 port magnetic	'\700ev\B 2 port\'
700eV, 2 port electrostatic	'\700ev\E 2 port\'
1000eV, 2 port nominal	'\1000ev\nom 2 port\'
1000eV, 2 port magnetic	'\1000ev\B 2 port\'
1000eV, 2 port electrostatic	'\1000ev\E 2 port\'
500eV, 4 port nominal	'\500ev\nom 4 port\'
500eV, 4 port magnetic	'\500ev\B 4 port\'
500eV, 4 port electrostatic	'\500ev\E 4 port\'
700eV, 4 port nominal	'\700ev\nom 4 port\'
700eV, 4 port magnetic	'\700ev\B 4 port\'
700eV, 4 port electrostatic	'\700ev\E 4 port\'
1000eV, 4 port nominal	'\1000ev\nom 4 port\'
1000eV, 4 port magnetic	'\1000ev\B 4 port\'
1000eV, 4 port electrostatic	'\1000ev\E 4 port\'
1000eV, 7 port nominal	'\1000ev\nom 7 port\'
1000eV, 7 port magnetic	'\1000ev\B 7 port\'
1000eV, 7 port electrostatic	'\1000ev\E 7 port\'

APPENDIX C
Typical Parameters for LAPD Plasmas and Ion Beam Operation

Magnetic field, B	0.7 kG
Pressure, P	$2x10^{-4}$ Torr
Electron density in afterglow, n_e	$1 \cdot 10^{11}$ cm^{-3}
Electron density in Discharge, n_e	$2.5 \cdot 10^{12}$ cm^{-3}
Neutral density, n_0	$6 \cdot 10^{11}$ cm^{-3}
Electron temperature in afterglow, T_e	0.1 eV
Electron temperature in Discharge, T_e	3 eV
Ion temperature in afterglow, T_i	0.1 eV
Ion temperature in Discharge, T_i	1 eV
Plasma column length	18 m
Plasma column diameter	70 cm
Cathode-anode discharge current	4 kA
Cathode-anode discharge frequency	1 Hz
Afterglow time	50 -60 ms
Discharge time	10 ms
Flux rope discharge voltage	160 V
Beam energy, W	500 - 1000 eV
Beam current density, j	~100 $\mu A/cm^2$
Beam size	0.5 cm Dia.
Pitch angle, θ	45.3 – 65.4°
Gyro-radius of fast ions, ρ	10.16 – 13.96 cm
Emitter voltage	700 V
Accelerator voltage	- 100 V
Energy spread, ΔE	~15 eV
Beam divergence	~5 degrees

References

[1] W. Gekelman, E. Lawrence, A. Collette, S. Vincena, B. Van Compernolle, P. Pribyl, M. Berger and J. Campbell, *Physica Scripta* **T142**, 014032 (2010).

[2] E. Lawrence and W. Gekelman, *Physics Review Letters* **103**, 105002 (2009).

[3] B. Van Compernolle and W. Gekelman, *Physics of Plasmas* **19**, 102102 (2012).

[4] B. Van Compernolle, W. Gekelman, P. Pribyl and C. Cooper, *Physics of Plasmas* **18**, 123501 (2011).

[5] W. Gekelman, B. Van Compernolle, T. DeHaas and S. Vincena, *Plasma Physics and Controlled Fusion* **56**, 064002 (2014).

[6] W. Gekelman, H. Pfister, Z. Lucky, J. Bamber, D. Leneman and J. Maggs, *Rev. Sci. Instrum.* **62**, 2875 (1991).

[7] W. W. Heidbrink, H. Boehmer, R. McWilliams, A. Preiwisch, Y. Zhang, L. Zhao, S. Zhou, A. Bovet, A. Fasoli, I. Furno, K. Gustafson, P. Ricci, T. Carter, D. Leneman, S. K. P. Tripathi and S. Vincena, *Plasma Physics of Controlled Fusion* **v54**, 124007 (2012).

[8] R. H. Huddlestone and S. L. Leonard, Plasma Diagnostic Techniques, New York: Academic Press, 1965.

[9] E. T. Everson, P. Pribyl, C. G. Constantin, A. Zylstra, D. Schaeffer, N. L. Kugland and C. Niemann, *Rev. of Sci. Instr.* **80**, 113505 (2009).

[10] "Model 101142 Alkali Ion Source," Heatwave Labs Inc., [Online]. Available: http://www.cathode.com/pdf/tb-118.pdf. [Accessed 23 August 2015].

[11] Y. Zhang, H. Boehmer, W. W. Heidbrink, R. McWilliams, D. Leneman and S. Vincena, *Rev. Sci. Instrum.* **78**, 013302 (2007).

[12] L. Zhao, W. W. Heidbrink, H. Boehmer, R. McWilliams, D. Leneman and S. Vincena, *Physics of Plasmas* **12**, 052108 (2005).

[13] S. Zhou, W. W. Heidbrink, H. Boehmer, R. McWilliams, T. A. Carter, S. Vincena, S. K. P. Tripathi and B. Van Compernolle, *Physics of Plasmas* **19**, 055904 (2012).

[14] B. Van Compernolle, W. Gekelman, P. Pribyl and C. Cooper, "Studies of a plasma with a hot dense core in LAPD," in *American Physical Society, 51st Annual Meeting of the APS Division of Plasma Physics, November 2-6, 2009, abstract #GP8.145* (2009).

[15] S. Zhou, W. W. Heidbrink, H. Boehmer, R. McWilliams, T. Carter, S. Vincena, S. K. P. Tripathi, P. Popovich, B. Friedman and F. Jenko, *Physics of Plasmas* **17**, 092103 (2010).

[16] S. Zhou, W. W. Heidbrink, H. Boehmer, R. McWilliams, T. A. Carter, S. Vincena and S. K. P. Tripathi, *Physics of Plasmas* **18**, 082104 (2011).

[17] Y. Zhang, W. W. Heidbrink, S. Zhou, H. Boehmer, R. McWilliams, T. A. Carter, S. Vincena and M. K. Lilley, *Physics of Plasmas* **16**, 055706 (2009).

[18] Y. Zhang, W. W. Heidbrink, H. Boehmer, R. McWilliams, S. Vincena, T. Carter, W. Gekelman, D. Leneman and P. Pribyl, *Physics of Plasmas* **15**, 102112 (2008).

[19] T. Hauff, M. J. Pueschel, T. Dannert and F. Jenko, *Physics Review Letters* **102**, 075004 (2009).

[20] A. Bovet, A. Fasoli, P. Ricci, I. Furno and K. Gustafson, *Physics of Fluids* **91**, 041101 (2015).

[21] A. Bovet, A. Fasoli and I. Furno, *Physics Review Letter* **113**, 225001 (2014).

[22] A. Bovet, I. Furno, A. Fasoli, K. Gustafson and P. Ricci, *Plasma Physics of Controlled Fusion* **55**, 124021 (2013).

[23] A. Bovet, I. Furno, K. Gustafson and P. Ricci, *Nuclear Fusion* **52**, 094017 (2012).

[24] A. H. Boozer and G. Kuo-Petravic, *Physics of Fluids* **24**, 851 (1981).